ORNL/Sub/87-SA946/08

# Properties and Performance of Ceramic Composite Components

April 9, 2001

Report Prepared by
R. H. Carter, M. Wone, S. W. Case, and K. L. Reifsnider
Department of Engineering Science and Mechanics
Virginia Polytechnic Institute and State University
Blacksburg, VA 24061

under
Subcontract Number 19X-SA496C

for

OAK RIDGE NATIONAL LABORATORY
Oak Ridge, Tennessee 37831
Managed by
UT-BATTELLE, LLC
for the
U. S. DEPARTMENT OF ENERGY
under contract DE-AC05-00OR22725

ORNL/Sub/87-SA946/08

# Properties and Performance of Ceramic Composite Components

April 9, 2001

Report Prepared by
R. H. Carter, M. Wone, S. W. Case, and K. L. Reifsnider
Department of Engineering Science and Mechanics
Virginia Polytechnic Institute and State University
Blacksburg, VA 24061

under
Subcontract Number 19X-SA496C

for

OAK RIDGE NATIONAL LABORATORY
Oak Ridge, Tennessee 37831
Managed by
UT-BATTELLE, LLC
for the
U. S. DEPARTMENT OF ENERGY
under contract DE-AC05-00OR22725

# TABLE OF CONTENTS

# 1. Introduction[†]

The objective of the Fossil Energy Advanced Research and Technology Development (AR&TD) Materials program is to conduct research and development on materials for longer-term fossil energy applications as well as for generic needs of various fossil fuel technologies. These needs have prompted research aimed toward a better understanding of material behavior in fossil energy environments and the development of new materials capable of substantial enhancement of plant operations, reliability, and efficiency.

The research program of the Materials Response Group at Virginia Tech addresses the need for reliable and durable ceramic composites to perform in high temperature applications. Areas of current research are characterization of oxide/oxide hot gas filter tubes and dense Nextel/SiC tubes. The focus of this report will be on the characterization of the Nextel/SiC tubes. In Section 2, we discuss the tube responses to axial tensile and compression loading as well as to torsional loading. Internal pressure test procedures are detailed and refinements are proposed. In Section 3, the elasticity theory model and nonlinear regression analysis currently being developed will be explained and preliminary results presented.

Finally, we have been working toward the goal of developing models for the strength and toughness of fibril-reinforced composites. The first step toward this goal, described in the last report and summarized in Section 3, is to develop models for the bridging stresses in cases in which the bridging fibers are randomly oriented. This model has been extended to include the effect of fiber length, and is used to determine the apparent toughness of a fibril-reinforced composite.

[†] Research sponsored by the U. S. Department of Energy, Fossil Energy Advanced Research and Technology Development Materials Program, DOE/FE AA 15 10 10 0, Work Breakdown Structure Element VPI-1

## 2. Performance of Nextel/SiC Composite Tubes

Improvements to fossil energy power facilities require the development of advanced materials to withstand the higher operating temperatures and harsh conditions needed to boost efficiency. Ceramic composites are a prime candidate since they offer excellent high temperature properties of monolithic ceramics with improved toughness needed for these applications. Fabrication of these materials has proved to be difficult, since the high temperatures needed to sinter the constituents can degrade the physical properties of the composite as a whole. More recently, methods have begun to rely upon chemical vapor infiltration (CVI) to deposit the matrix material into the fiber performs. This allows for the formation of several different matrix and fiber systems without requiring the high processing temperatures seen in other processes. Unfortunately, standard CVI procedures require infiltration times that can be too long to be considered economically feasible.

Development of new processes has resulted in greatly reduced infiltration times, overcoming many of the problems of previous CVI techniques. The previous methods, such as isothermal/isobaric CVI, rely upon diffusion processes to deposit the matrix material. Low deposition rates were used to prevent large density gradients caused by the outer surfaces becoming fully dense, and not permitting infiltration to the inner portions. This results in the long deposition times or high porosity. Researchers at Oak Ridge National Laboratory (ORNL) have developed a new method to overcome the problems of long process times or large density gradients[1-4]. The forced flow-thermal gradient process (FCVI) utilizes a temperature gradient to change the deposition rates from the inner preform to the outer surface. The deposition times are reduced from a period of weeks to that of only hours, forming nearly dense composites without density gradients.

The process has been used to fabricate planar samples, and it has been scaled-up to produce samples with a tubular geometry. To determine the effectiveness of the process, the completed materials have been sent out for material characterization. Much of the previous mechanical testing of composites made using the FCVI technique has been limited to relatively small planar samples. These test methods include flexure tests and some limited axial testing[5-7]. With the larger sample size and different sample geometry, different tests need to be performed to characterize the mechanical properties of tubular samples. The Materials Response Group at Virginia Tech has performed testing on previous tubes supplied by ORNL and Babcock and Wilcox (now McDermott Technologies, Inc., Lynchburg, VA)[8-10]. That work focused on the mechanical properties of Nicalon/SiC and alumina/alumina ceramic composites of various designs and lay-ups. The materials were fabricated by different methods, ranging from using forced flow CVI for the Nicalon/SiC[10] to sol-gel processing to deposit an alumina matrix for the alumina/alumina materials[8,9]. The mechanical properties for these materials are listed in Table I.

The approach used in this study will be modeled after that applied in Carter, *et al* for characterizing hot gas candle filter tubes[11,12]. It is similar to the earlier work performed at Virginia Tech, in that, axial tension, compression and torsion are used to characterize the elastic response of the tubes. Internal pressurization tests have been developed and used to gain further insight into the behavior of these materials. Internal

pressure and axial/biaxial tensile strength tests are used to characterize the strength of the composites under different loading conditions.

**Table I. Reported properties from previous tube samples**

| Material | Axial Stiffness Tension (GPa) | Shear Stiffness (GPa) | Axial Strength (MPa) | Shear Strength (MPa) |
|---|---|---|---|---|
| Nicalon/SiC Braided tube[10] | --- | 127 | --- | --- |
| Nicalon/SiC Cloth wrapped[10] | ~275 | 94 | --- | --- |
| Almax/$Al_2O_3$[8,9] | 54-61 | 41-43 | 41.4, 44.5 | 56.54 |

## *2.1 Fabrication*

The composite tubes were fabricated using the forced-flow, thermal gradient chemical vapor infiltration technique at developed at Oak Ridge[2,3]. The preforms consisted of ten to twelve Nextel 610 (Nextel 312 for sample CVI-1173) braided sleeves stretched over a polyethylene mandrel. The green preform was infiltrated with a small amount of Borden Durite resin to provide some structural support prior to the silicon carbide infiltration. The preform was compressed by aluminum tube sections and allowed to cure. The cured preform was trimmed to a 35.5-cm length prior to the SiC infiltration via the FCVI process. The FCVI process conditions were as follow: 1200°C, 5 slm of hydrogen, and 1 slm of methyltrichlorosilane (MTS). The samples achieved 80 to 90% of theoretical densities in about 36 hours. Once processing was completed the ends of the samples were removed to leave a 30-cm long sample. The final tube properties are listed in Table II. It should be noted that in this study, no fugitive carbon layer was deliberately deposited to improve composite toughness. A small amount may be present from the decomposition of the resin used to rigidize the preform, though none was noticed in the initial inspection of the tubes.

**Table II. Properties of the Nextel/SiC composite tubes**

| | CVI 1173 | CVI 1216 | CVI 1219 |
|---|---|---|---|
| **Process Time(hours)** | 36 | 43 | 36 |
| **Density ($g/cm^2$)** | 3.00 | 2.88 | 3.08 |
| **% Theoretical Density** | 87 | 81.8 | 80.3 |
| **Fiber Type** | Nextel 312 | Nextel 610 | Nextel 610 |
| **Fiber Volume Fraction (%)** | 50 | 37.5 | 32.2 |
| **Number of layers** | 10 | 10 | 8 |

A cross section of the CVI-1173 tube can be seen in Figure 2-1. The light gray layer on the inner surface is a SiC layer deposited during the FCVI process. This layer was less than 1 mm at the ends of the tube, and approached 4 mm in thickness in some cross sections taken near the middle of the sample.

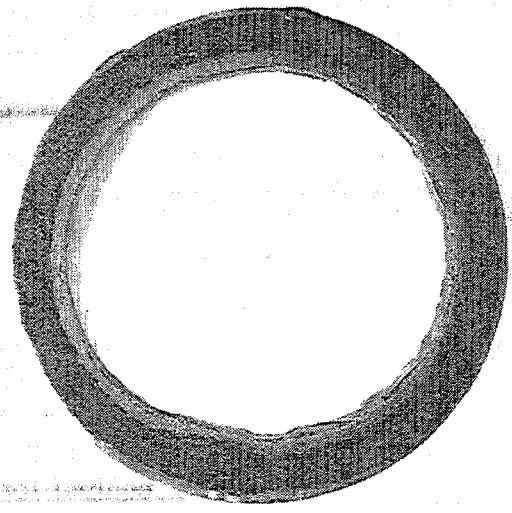

**Figure 2-1:** Cross section of sample 1173

The change in dimension creates problems in accurately calculating the stress in the material. The cross sectional area and polar moment of inertia used in this study were calculated from the average values of the outer diameter and tube thickness at each end of the sample. The average dimensions for the samples are in Table III. The changes in the dimensions of CVI 1219, shown in the last two columns, are due to changes made to the sample during testing. An excess layer of SiC was deposited on the inner surface, and, after the material strength exceeded the load capacity of the MTS system, it was machined out at ORNL. The wall thickness values for the sample after milling exhibits large variations, which is due to the inner surface not being concentric with the outer.

**Table III. Dimensions of the samples**

| *In mm* | **CVI 1173-1** | **CVI 1173-2** | **CVI 1216** | **CVI 1219** (as-received) | **CVI 1219** (after milling) |
|---|---|---|---|---|---|
| **Outer Diameter** | 59.7±0.2 | 59.7±0.2 | 59.3±0.06 | 59.2±0.1 | 59.1±0.2 |
| **Thickness** | 6.9±0.7 | 6.8±0.4 | 7.6±0.6 | 7.9±1.8 | 4.8±0.4 |
| **Inner Diameter** | 45.8 | 46.1 | 43.9 | 43.4 | 49.7 |
| **Area** ($*10^{-4}$ $m^2$) | 11.48 | 11.24 | 13.09 | 14.99 | 8.14 |

## 2.2 *Axial tests*

Axial tension, torsion and compression tests were performed on each of the samples using a MTS servo-hydraulic load frame with axial and torsional capabilities. The load ranges for the frame were ±246 kN (50 kip) in tension/compression and ±2.3 kN-m (20 in-kip) in torque. The Teststar II software from MTS handled system control and data acquisition. This allowed the recording of all loads, displacements, and strains from the strain gages, simultaneously.

To increase the number of samples, CVI 1173 was cut in half to provide two axial samples approximately 15-cm in length. The later samples, CVI 1216 and 1219, were sectioned differently to provide internal pressure test samples. From each of the tubes, two 3.5 to 4.0-cm internal pressure test samples were cut from the initial sample, leaving a 23-cm sample for axial testing. For the CVI 1173 axial samples, the ends were initially potted in epoxy and machined down to acceptable tolerance for the MTS grips. The low stiffness of the epoxy proved insufficient to support the high compressive force in the grips. Both of the 1173 axial samples suffered grip-induced failures. For samples CVI 1216 and 1219, 6.25-cm long steel inserts were made to closely fit into the tube ends and were bonded in place with epoxy to provide support. Again, the outer surface was built up with epoxy and milled down to the tolerances required for the MTS grips. Grip related failures have not been observed on either sample using this configuration.

Strain measurements were made using four strain gage rosettes equally spaced around the samples, as can be seen in Figure 2-2. The redundant measurements are made to account for any specimen misalignment, since small misalignments can generate significant stress/strain variations through the sample. In the elastic regime (below matrix cracking), these effects can be removed by averaging the stain values. A typical axial stress/strain curve is located in Figure 2-3. The plotted values are the average of the different strain components from each gage. The recording of the different strain components (axial, hoop, and shear) is important for the analysis being developed and is explained in Section 3. Table IV contains the measured mechanical properties of the tubes. The stiffness values are calculated from the strain data collected from the strain gages and the nominal stress values (calculated using the average values for the area and polar moment of inertia).

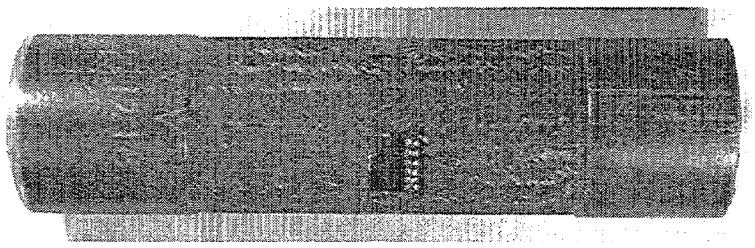

**Figure 2-2**: Specimen configuration for axial tube testing.

The two sets of elastic values listed for both CVI 1216 and 1219 are due to the changes made in the samples after the first series of tests, where neither sample failed in tension. For both samples, the SiC layer on the inner surface of the tube was relatively thick (on the order of 4-mm thick for CVI 1219), increasing the cross-sectional area, thereby decreasing the stress in the material during testing. Due to this, the strength of

the sample exceeded the load capacity of the MTS system (246 kN). The steel inserts were removed by burning off the epoxy layer by placing the sample in a furnace at 400°C for 1 hour. The power was turned off, and the system was allowed to cool over night before the sample was removed. The epoxy burned off leaving the samples coated in charred epoxy resin and soot, but free of the inserts. The SiC layer on CVI 1216 was too

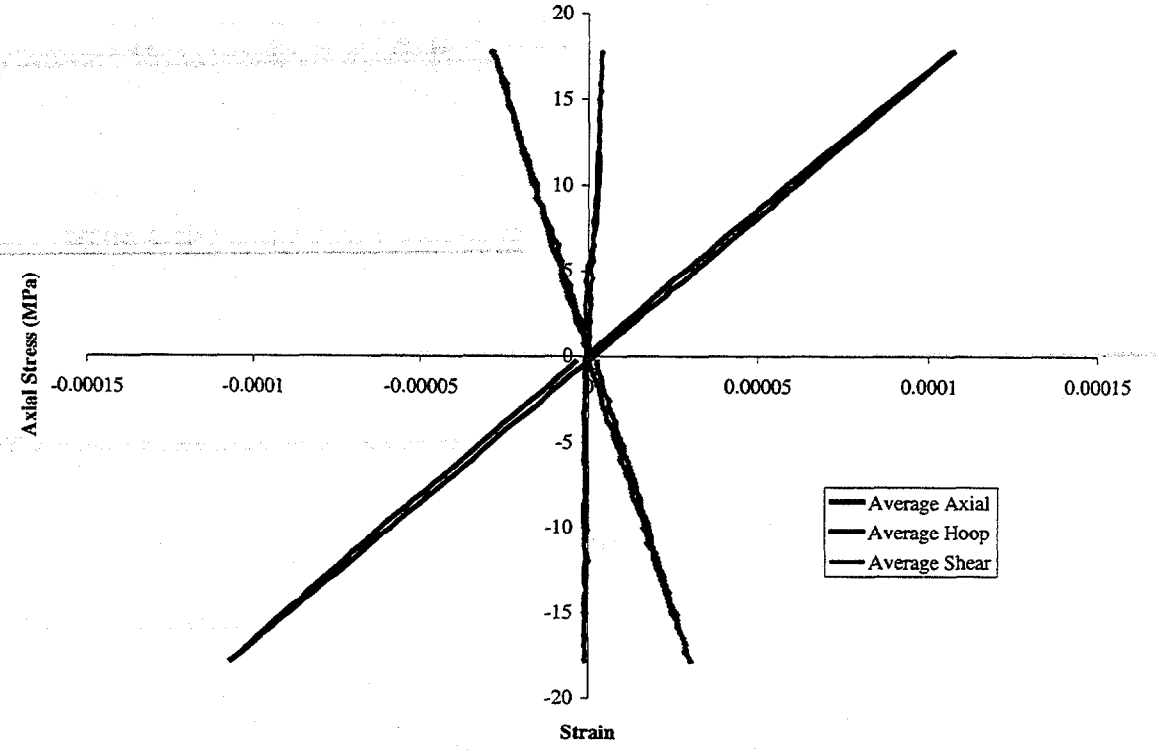


**Figure 2-3: Typical tensile test.**

thin for effective machining without damaging the sample, so it was repotted and returned to testing. CVI 1219 was returned to ORNL, and the SiC layer was machined off the inner surface. For Sample CVI 1216 – AR is for As-Received and AHT is for After Heat Treatment. For Sample CVI 1219 – AR is for As-Received and AM for After-Milling.

The axial stiffness for CVI 1216 was not affected by the thermal exposure to remove the epoxy, while the torsional stiffness increased by 28%. The torsional tests have been repeated, with little variation in the observed modulus. Investigation into what structural changes may have occurred has not been conducted at this point. The properties for CVI 1219 increased slightly with the removal of the SiC inner coating.

The stress/strain curves for the tensile strength tests of the CVI 1173 samples are in Figure 2-4. The tensile strength values for the two 1173 samples are not indicative of the material since both exhibited grip induced failures. Both 1173 samples exhibited a small amount of nonlinear behavior, as can be seen in the departure from the CVI 1216 line. The fracture surface exhibited some fiber pullout, as can be seen in Figure 2-10. CVI 1219 failed in the gage section, and the tensile strength plot is in Figure 2-5. An

extension of the linear behavior of the material is included to illustrate the nonlinear behavior.

**Table IV:** Mechanical Properties of the Nextel/SiC composite tubes

| Tube ID | Axial Stiffness (GPa) | Torsional Stiffness (GPa) | Poisson Ratio | Tensile Strength (MPa) |
|---|---|---|---|---|
| **1173-1** | 172.5 | 66.1 | 0.25 | 31.1 |
| **1173-2** | 165.2 | 65.7 | 0.24 | 68.1 |
| **1216** AR | 168.1 | 62.8 | 0.20 | >171.5 |
| **1216** AHT | 167.5 | 80.17 | 0.27 | >197.4 Axial + 43.5 Shear |
| **1219** AR | 142.1 | 65.1 | 0.31 | >137 |
| **1219** AM | 148.8 | 67.3 | 0.52 | 200.2 |

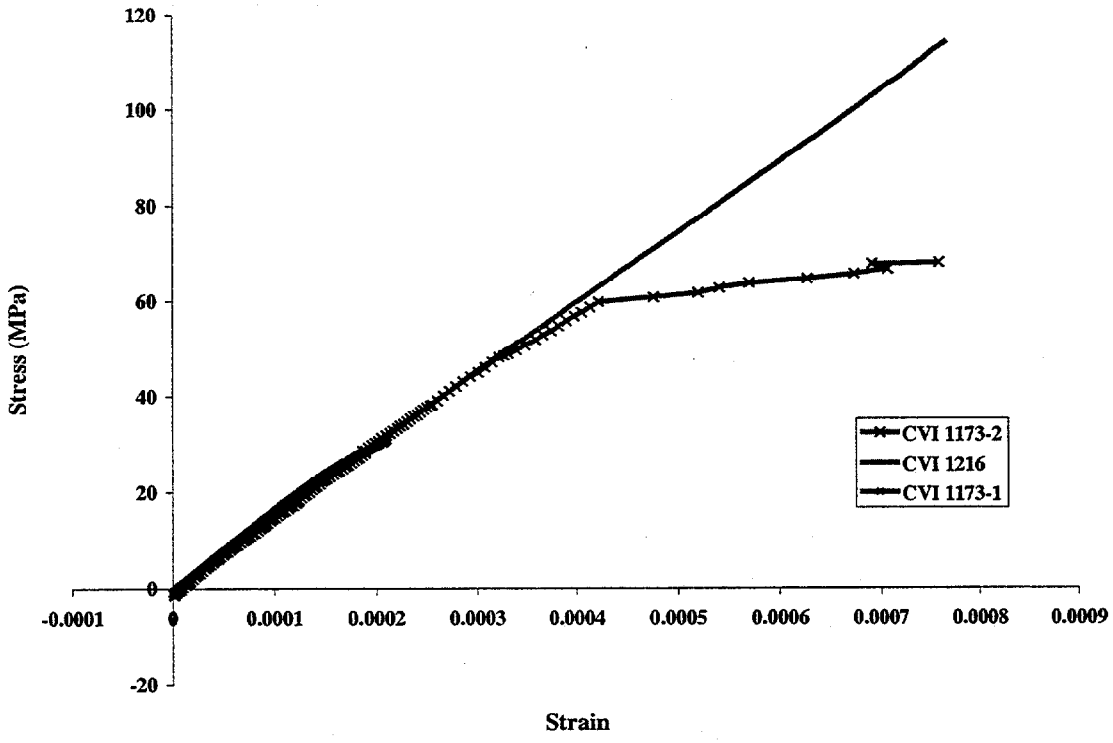


**Figure 2-4: Stress/ Axial Strain curves for tensile strength tests**

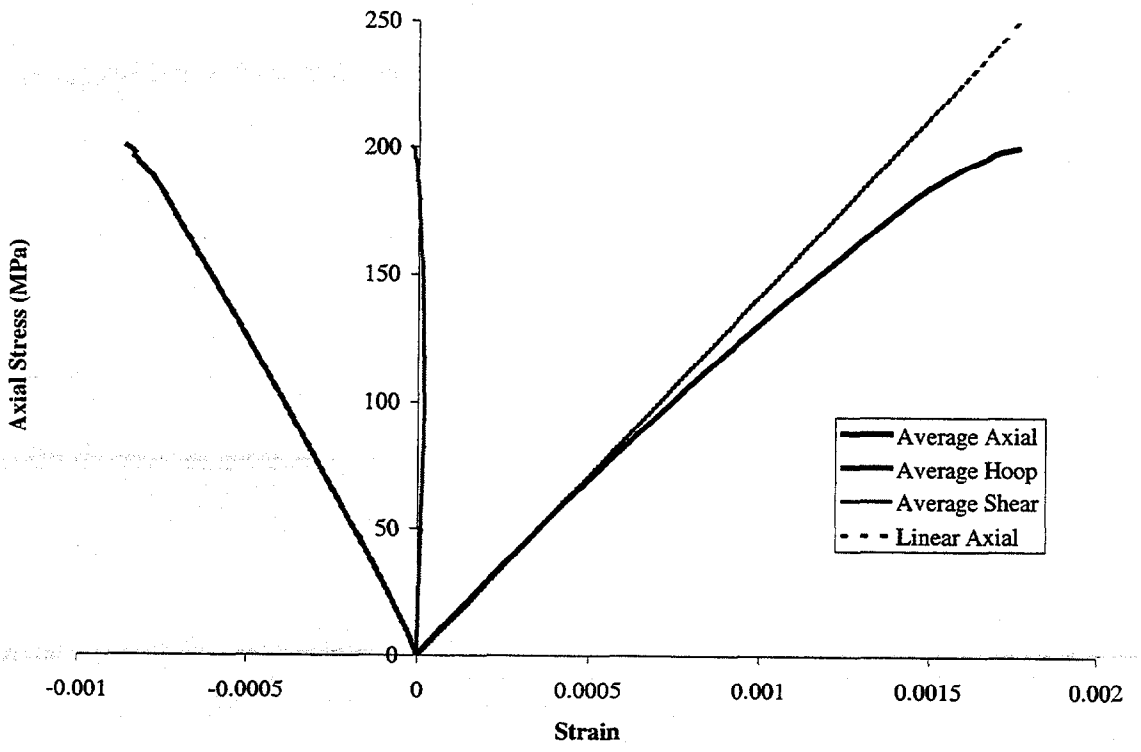


**Figure 2-5. Tensile Strength Plot for CVI 1219.**

During the testing of samples 1216 and 1219 AR, the load profile reached the system limit before failure. The values listed are the largest nominal stress values applied before the 246 kN (55 kip) limit or prior to slippage of the sample. In order to test CVI 1216 and 1219, the grip pressure was boosted to 38 MPa, from the normal setting of 20 MPa, to prevent slipping at the higher loads. For CVI 1216 AHT, the load profile was altered so that torque would be applied when the axial load limit was reached. The load profile for CVI 1216 is in Figure 2-6. The axial force reaches 246 kN and an applied torque of 1422 N-m before the sample slipped out of the grips of the MTS frame. Later attempts to repeat the test to a higher level failed due to wear on the epoxy grip surface.

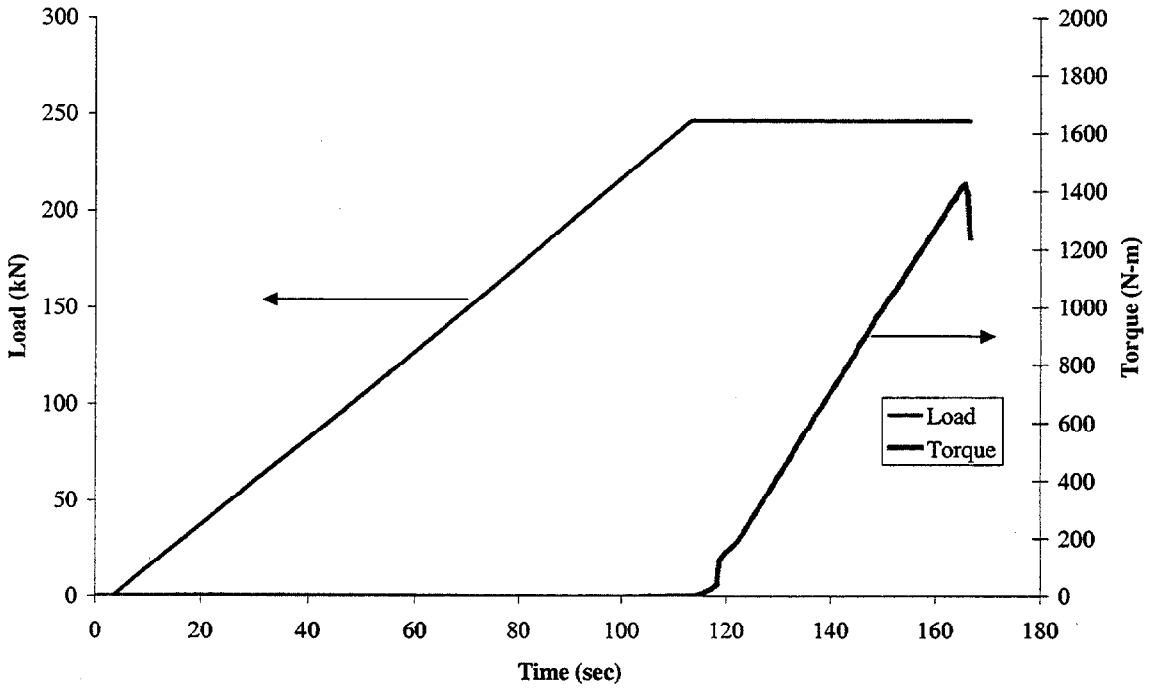


**Figure 2-6. Load Profile for CVI 1216**

Figure 2-7 and Figure 2-8 are of the strain response to the different sections of the loading profile. Figure 2-7 has the pure tension results, while 2-8 contains the result for the torque ramp with a constant 246 kN axial load.

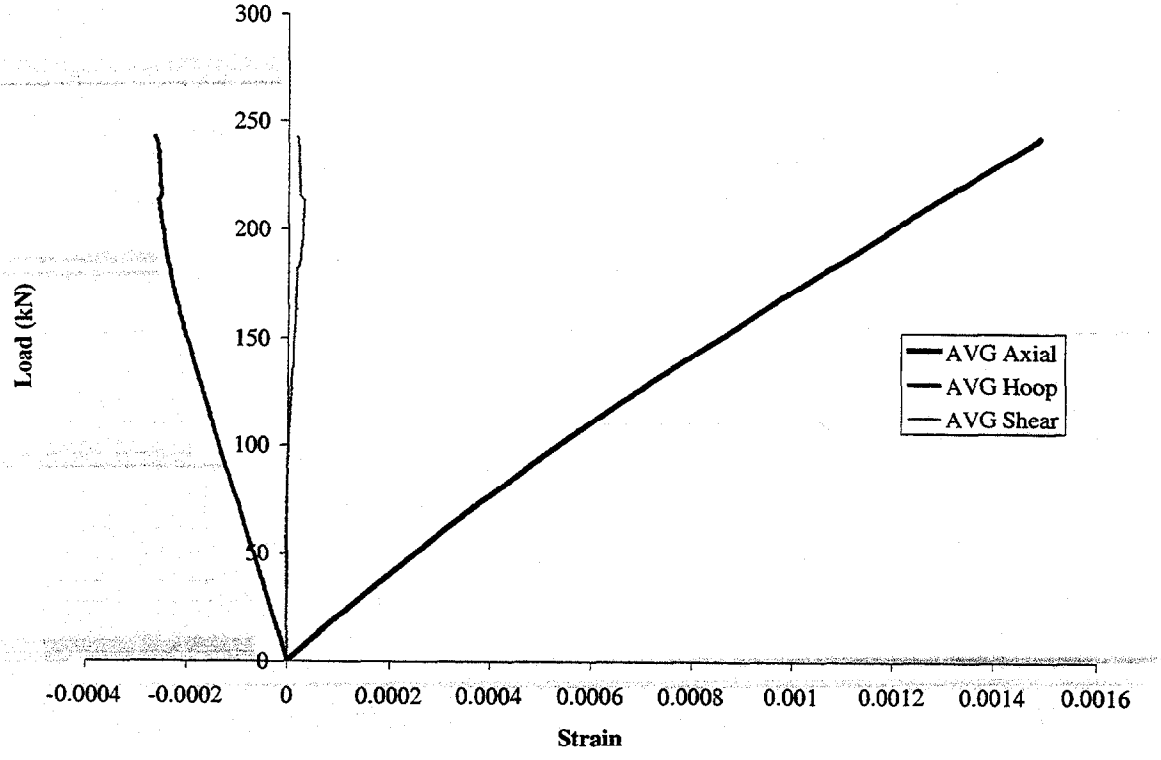


**Figure 2-7. Strain response for the tension only portion of Figure 2-6**

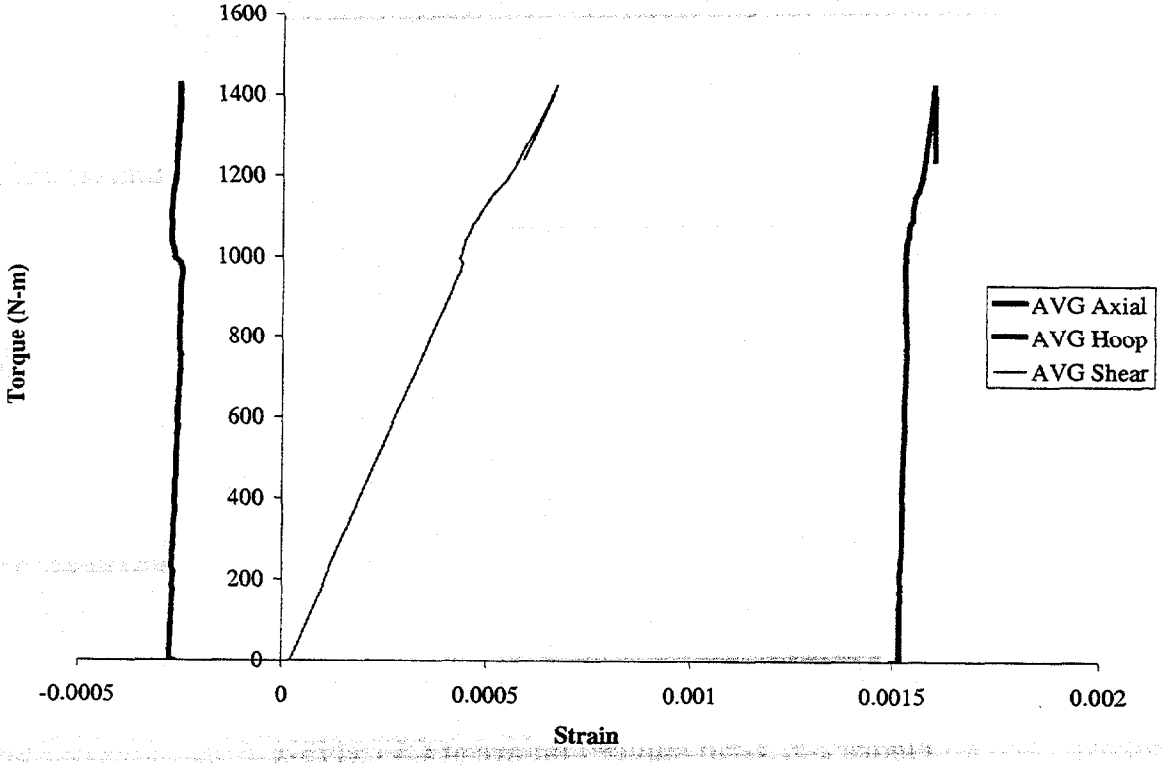


**Figure 2-8. Strain response for the torque ramp with 246kN load**

Photographs of the failed of samples CVI 1173-1 and CVI 1219 are in Figure 2-9 through Figure 2-12. The first two images show the grip-induced failure of the CVI 1173-1. The failure originated in the region above the grip area, as can be seen in Figure 2-9. Figure 2-11 and Figure 2-12 are of CVI 1219. All the samples exhibited fiber pullout, while CVI 1219 had delamination and pullout (highlighted in Figure 2-11).

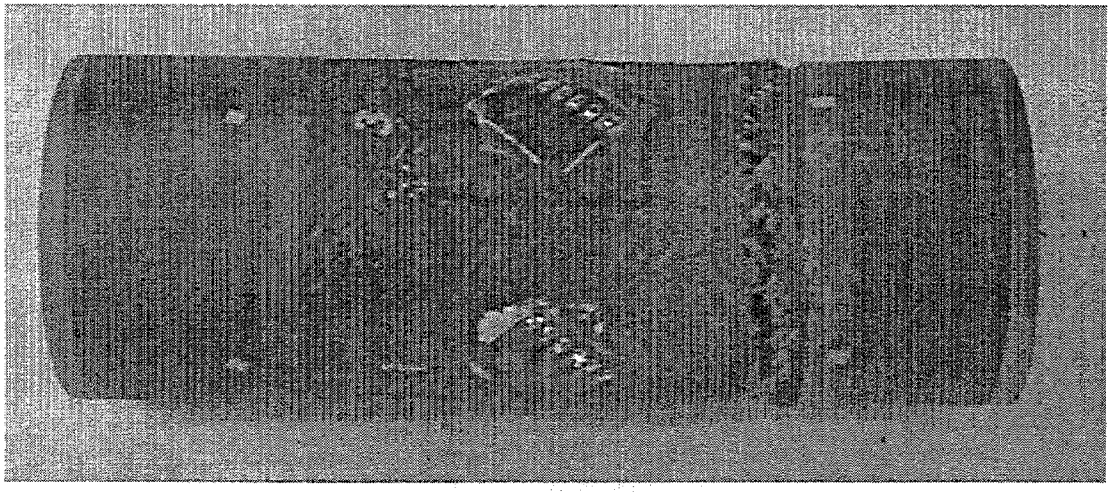

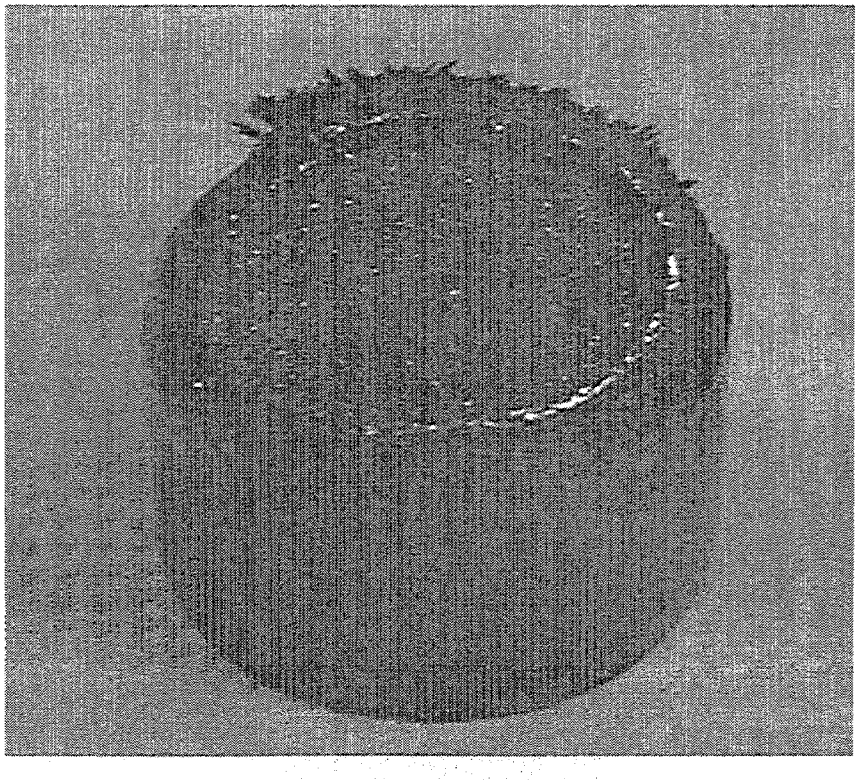

**Figure 2-9. Grip induced failure of CVI 1173-1**

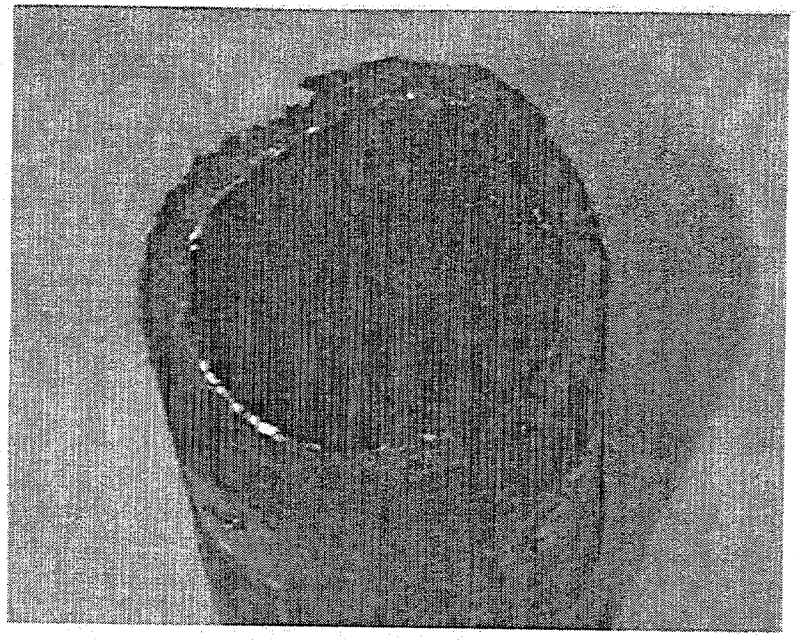

**Figure 2-10: Fractured tensile strength specimen CVI 1173-1**

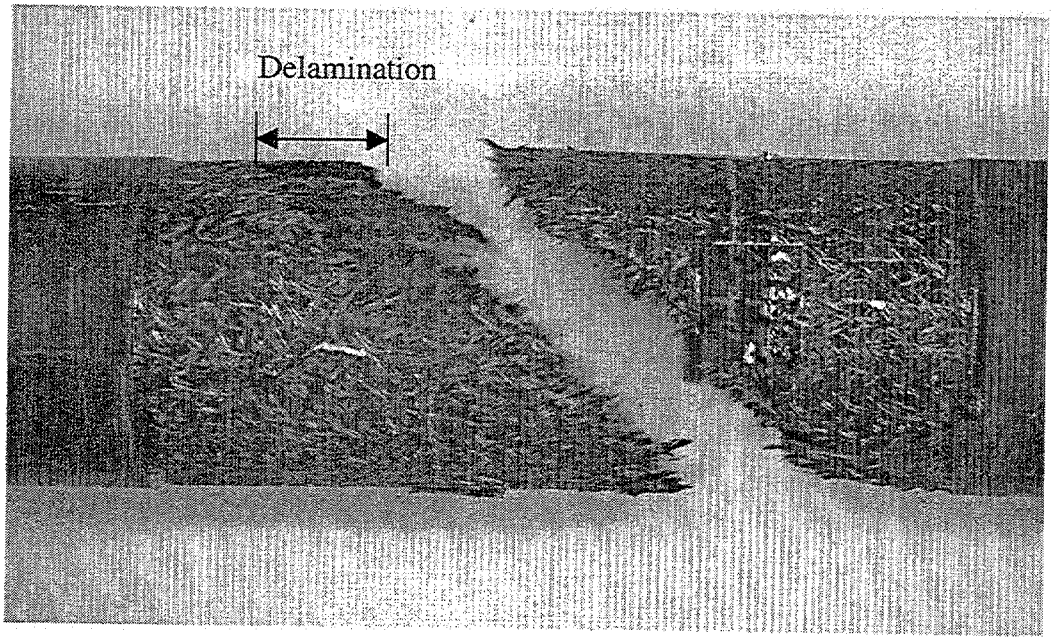


**Figure 2-11. Sample CVI 1219 with large amounts of fiber pullout and delamination**

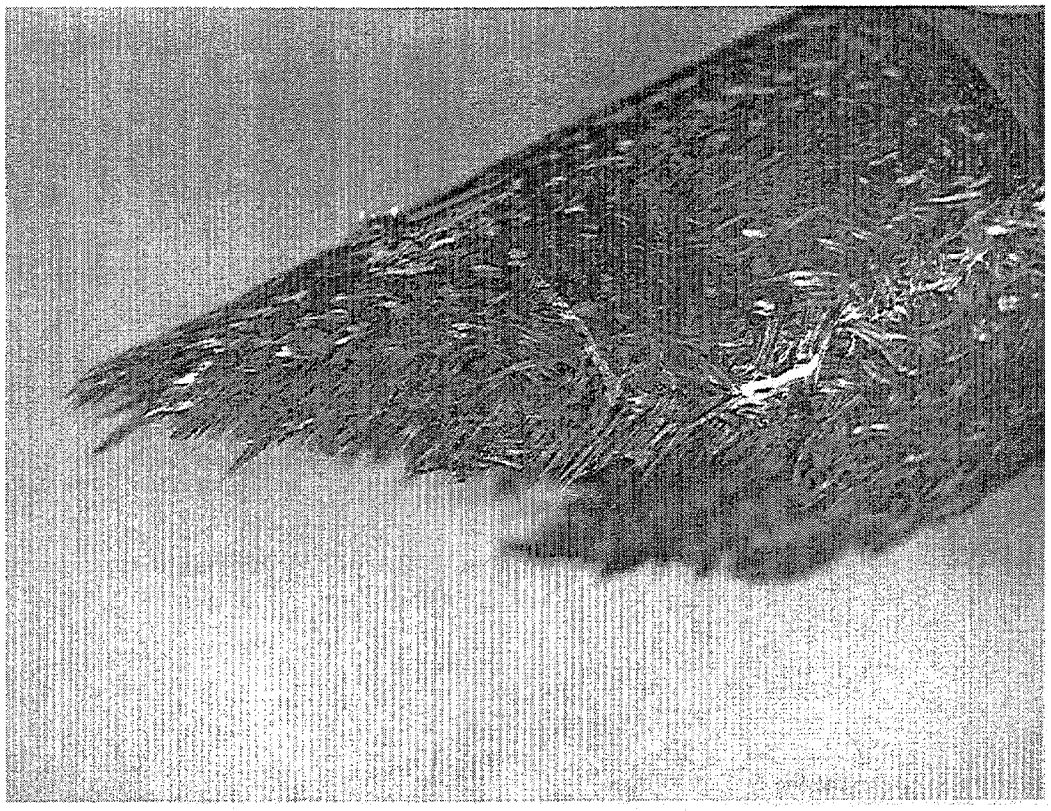

**Figure 2-12. Sample CVI 1219 failure surface with pullout**

## 2.3 *Internal pressure tests*

Internal pressure testing is a common method used for characterizing composite tubes[11-15]. The method generates stress in the material primarily in the hoop direction of the sample. This provides more information on the properties of the material when used with axial tests. The procedure used the compressed rubber plug technique as described

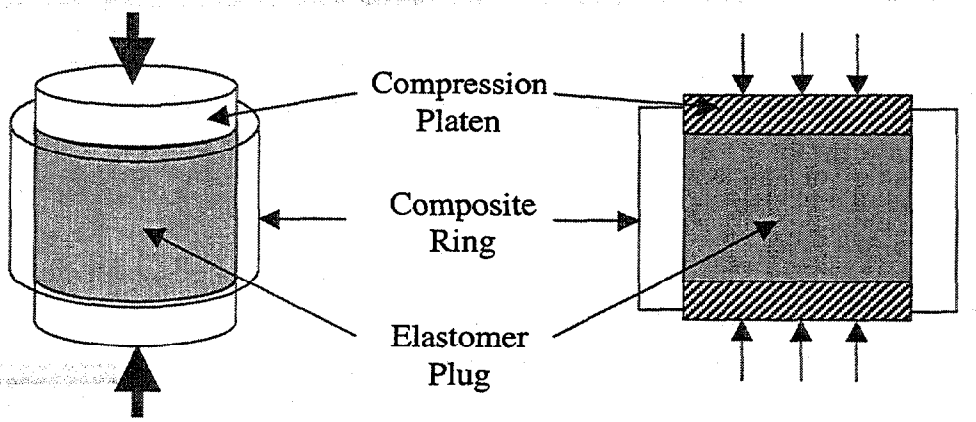


**Figure 2-13:** Schematic of internal pressure test with cross-section

in Singh, *et al*[13]. A schematic of the test is in Figure 2-13. By compressing the rubber plug, the Poisson expansion of the material will generate pressure on the inner surface. The internal pressure is calculated by the expression:

$$P_i = \frac{\sigma_p - E_p \varepsilon_z}{2\nu_p} \tag{2.1}$$

Where $P_i$ is the internal pressure, $\sigma_p$, $E_p$, $\varepsilon_z$ and $\nu_p$ are the compressive stress, Young's modulus, axial strain, and Poisson's ratio for the plug material. This expression is derived from an elasticity solution for an isotropic, linear elastic material. Due to the axisymmetric loading conditions, the radial and hoop stress are equal throughout the plug[16]. With this information, Hooke's Law can be rearranged into the expression above. It is important to note that due to the large deformations used for these tests (20 to 30% on average), true stress and strain values should be used for this procedure. These values are found from the engineering stress and strain values by:

$$\begin{aligned} \tilde{\varepsilon} &= \ln(1+\varepsilon) \\ \tilde{\sigma} &= \sigma(1+\varepsilon) \end{aligned} \tag{2.2}$$

where $\tilde{\sigma}$ and $\tilde{\varepsilon}$ are the true stress and strain and $\sigma$ and $\varepsilon$ are the engineering stress and strain[17].

The elastomer compound used for these tests was Dow Corning Silastic silicone rubber (Silastic T-2). Initial work with this material was unsuccessful, due to the material

failing by shearing out around the compression platens. Later attempts used a urethane rubber compound, which exhibited better shear properties. Difficulties arose with accurately predicting the pressure generated due to the nonlinear elastic and viscoelastic properties of the urethane. The Silastic compounds were re-examined and found to exhibit linear elastic behavior with no appreciable viscoelastic effects. The compression platens were made to match the inner diameter of the sample more closely, which eliminated problems with the shear deformations and failure of the plug.

A high-pressure lubricant is applied to the plug, platen, and inner surface of the sample to minimize compressive loads generated by friction and to generate a more uniform internal pressure. After each test, the plug and sample are inspected for any damage associated with the test. To date, the tests have not been run to a level sufficient to damage the SiC composites. New elastomeric compounds are being investigated, and the procedures are being improved in the hope of increasing the pressure above the strength of the material.

To validate this procedure and check whether the pressure calculated and generated were the same, a pressure test was performed on a stainless steel sample. The steel used was an AISI Type 304 stainless steel with a Young's modulus of 193 GPa. The pressure was calculated by linear elastic equations (Equations 2.1 and 2.2), by hyper-elastic equations, and by the Lamé cylinder solution for a homogenous, isotropic material. There are several different equation to describe hyper-elastic materials, but the Mooney-Rivlin equations were found to adequately describe the behavior of the Silastic material[15,18]. The Mooney-Rivlin equations describing the deformations of hyper-elastic materials are:

$$f = 2\left(\lambda - \frac{1}{\lambda^2}\right)\left(C_1 + \frac{C_2}{\lambda}\right) \tag{2.3}$$

where $f$ is the force per unit unstrained area ($\sigma_o$), $C_1$ and $C_2$ are material constants, and $\lambda^2=(1+\varepsilon)^2$. For the linear elastic and hyper-elastic equations, the stress value calculated is that for an unconstrained plug compression, which occurs early in the internal pressure test prior to contact with the sides of the sample. Assuming that the Silastic is incompressible and possesses a Poisson's ratio of 0.5, once contact is made the axial stress in the plug is the unconstrained stress plus the pressure generated on the wall of the sample, or:

$$\sigma_{axial} = \sigma_{unconstrained} + p_i \tag{2.4}$$

This allows for the pressure to be calculated by removing the elastic stress contribution of compressing the plug from the measured applied stress.

To apply the Lamé cylinder solution, the frictional loading was neglected, and the hoop stress was calculated from the strain gage measurements ($\sigma_\theta=E\varepsilon_\theta$). The value of the hoop stress at the outer radius of the sample is:

$$\sigma_\theta = \frac{2r_i^2 p_i}{r_o^2 - r_i^2} \tag{2.5}$$

which can be rearranged to solve for pressure:

$$p_i = \frac{\left(r_o^2 - r_i^2\right)\sigma_\theta}{2r_i^2} \tag{2.6}$$

where $r_i$ and $r_o$ are the inner and outer radii, $p_i$ is the pressure, and $\sigma_\theta$ is the hoop stress[16].

With this information, the test results for the stainless steel sample are in Figure 2-14. The graph is of the pressure calculated vs. the compressive strain of the rubber plug. All methods find similar values for the pressure generated in the test. The flatter portion of the curves, between –0.14 to –0.18 strain, is believed to be due to friction between the sample and the plug, since the pressure is least accurate during that portion of the test. Different lubricants are currently being tested to reduce the friction effects.

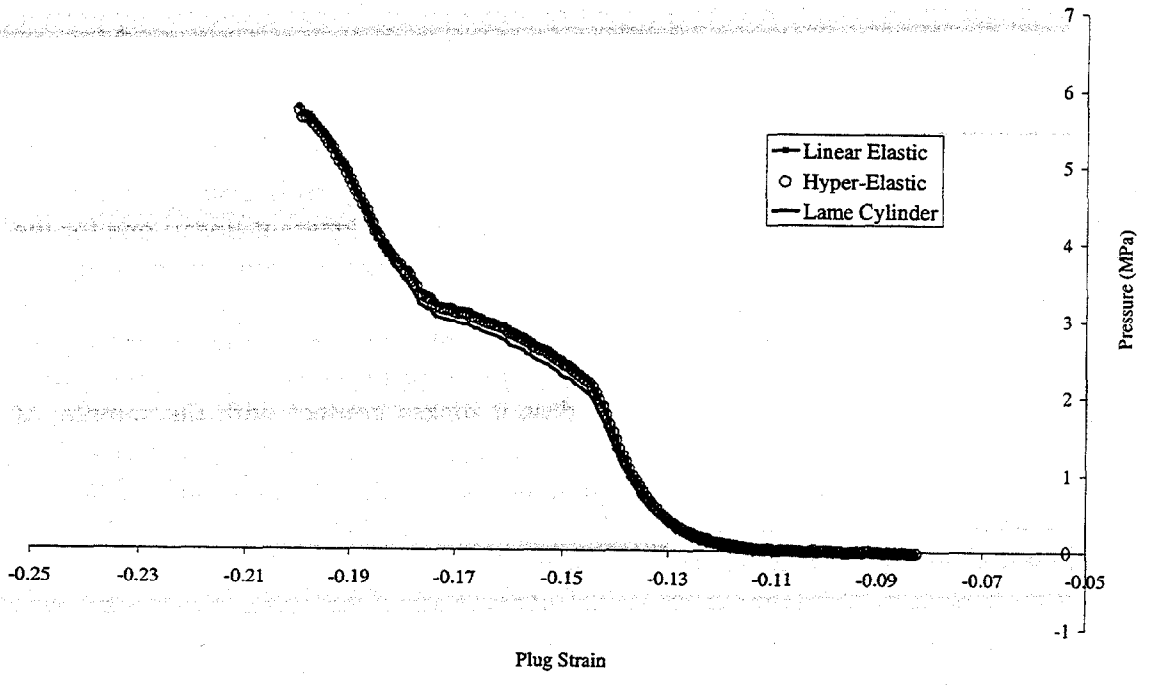


**Figure 2-14. A comparison of the different method to calculate the internal pressure for a stainless steel control sample.**

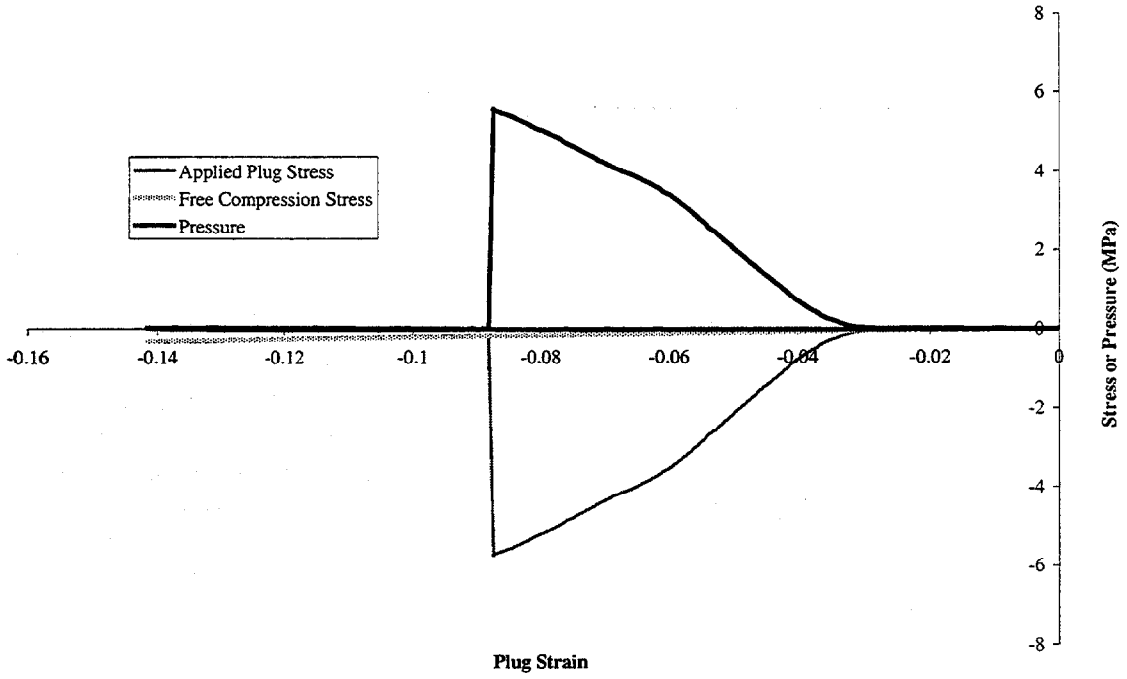


**Figure 2-15. Stress and Pressure curves for an internal pressure test**

Another test of this method can be seen in Figure 2-15, which is an internal pressure test for a carbon/epoxy composite tube. This figure contains three different lines: one for the Free Compression Stress, the Applied Plug Stress, and the Pressure (calculated using the elastic equations). The free compression stress is the linear elastic curve of an unconstrained plug, while the applied plug stress is stress measured during the test (a constrained plug). The difference of the two is the pressure to the sample. In the graph, above 3% strain, the plug becomes constrained as it makes contact with the sample, as seen by the rapid rise in the applied stress. Around 9% strain, the sample fails, returning the applied stress to that of the unconstrained or free compression levels. The test reached a maximum of 14% compressive strain, and then returned to zero, with both the free compression and applied stress lines overlapping.

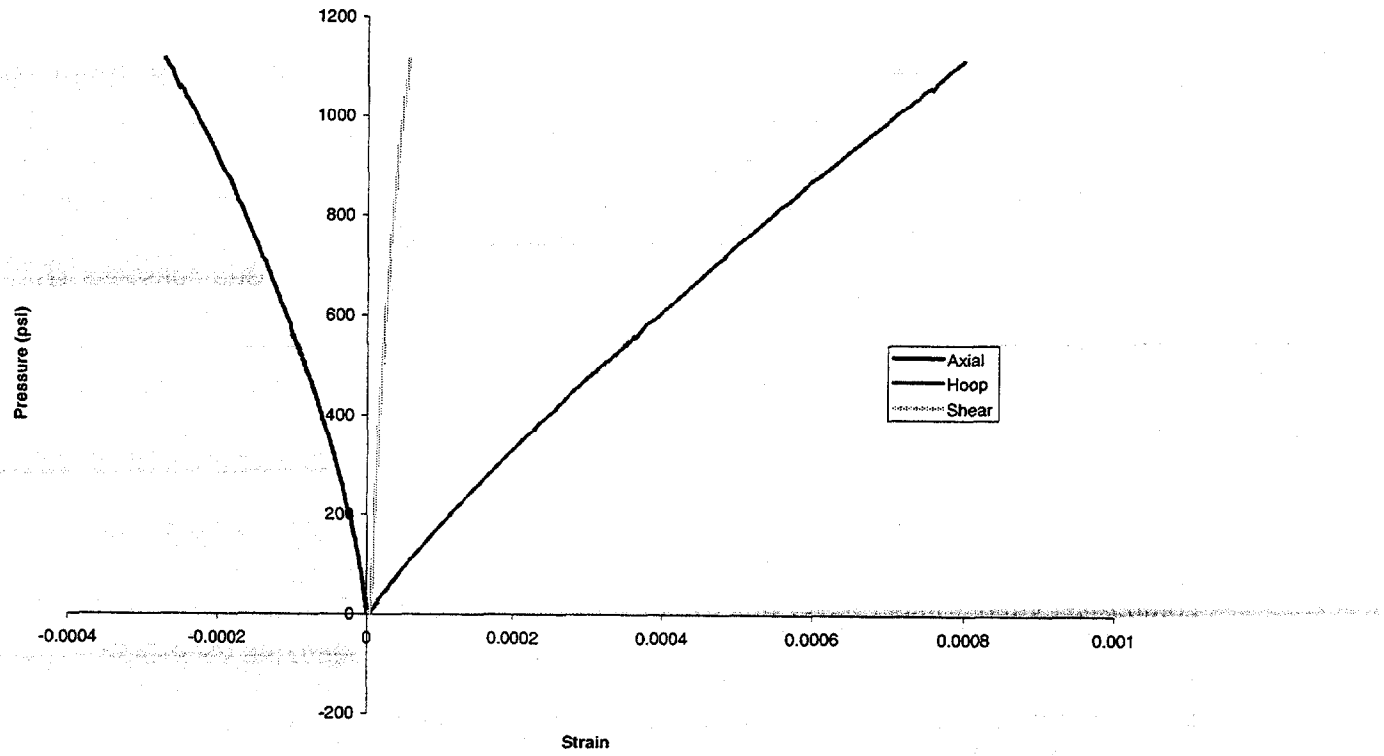


**Figure 2-16. Measured strain vs. internal pressure for an internal pressure test (Sample CVI 1219).**

The results of the internal pressure tests are in Table V. The values are the slopes found by linear regression for the data, as shown in Figure 2-16 (Pressure/strain). Others in the literature have calculated the hoop stress in the cylinder due to the internal pressure by expressions from elasticity theory (Lame's Cylinder solution)[14]. This assumes a homogenous, isotropic material behavior, which is not expected with these materials, but will be used here to describe the results. Work described in the next section is being developed to address the problem of finding a better method to represent the results to internal pressure tests, since these materials are neither homogenous nor isotropic.

**Table V. Slopes of the best-fit data for CVI 1219**

| Values | Axial (GPa) | Hoop (GPa) | Shear (GPa) | Poisson's ratio |
|---|---|---|---|---|
| **Pressure/Strain** | -66.4 | 12.3 | 89.4 | 0.18 |
| **Hoop Stress/Strain** | -348.6 | 64.4 | 469.4 | 0.18 |

## 3. Analysis of Data

So far, the characterization of the composite tubes has focused on the global responses (axial stiffness and strength, torsional stiffness, and internal pressure burst tests). A better understanding of the material would come from knowing the ply-level elastic properties, but it is not possible to measure those directly for a composite tube. Current research is developing methods to determine the ply-level elastic constants ($E_1$, $E_2$, $E_3$, etc...) for a homogenous, orthotropic composite laminate. The first part of this section will review the elasticity solution for these structures subjected to axisymmetric loading conditions. In the second part, a nonlinear regression analysis will be detailed with some results.

### *3.1 Elasticity or "Forward" Solution*

The derivation illustrated is from the work by Rousseau, *et al*[19]. The following expressions can be used to calculate the stresses, strains and displacements for a composite cylinder under axisymmetric loading conditions (axial tension, compression, torsion, internal pressure and uniform temperature change). By applying the Strain-Displacement relations to the Displacement equations, the different strain components can be calculated through the thickness of the tube. The strain values are related to the stress values by the Constitutive equations.

**Displacement Equations** – u = axial displacement, v = tangential and w = radial displacement

$$
\begin{aligned}
u(x) &= \varepsilon^o x \\
v(x,r) &= \gamma^o x r \\
w(r) &= A_1 r^{\lambda} + A_2 r^{-\lambda} + \Gamma \varepsilon^o r + \Omega \gamma^o r^2 + \Psi r \Delta T \\
\lambda &= \sqrt{\frac{\bar{C}_{22}}{\bar{C}_{33}}} \\
\Gamma &= \left( \frac{\bar{C}_{12} - \bar{C}_{13}}{\bar{C}_{33} - \bar{C}_{22}} \right) \\
\Omega &= \left( \frac{\bar{C}_{26} - 3\bar{C}_{36}}{4\bar{C}_{33} - \bar{C}_{22}} \right) \\
\Psi &= \left( \frac{(\bar{C}_{i2} - \bar{C}_{i3})\alpha_i}{\bar{C}_{33} - \bar{C}_{22}} \right)
\end{aligned}
\qquad (3.1)
$$

**Strain-Displacement Equations**

$$\begin{aligned} \varepsilon_x &= \frac{\partial u}{\partial x} & \gamma_{r\theta} &= \frac{\partial v}{\partial r} - \frac{v}{r} = 0 \\ \varepsilon_\theta &= \frac{w}{r} & \gamma_{xr} &= \frac{\partial u}{\partial r} = 0 \\ \varepsilon_r &= \frac{\partial w}{\partial r} & \gamma_{x\theta} &= \frac{\partial v}{\partial x} + \frac{1}{r}\frac{\partial u}{\partial \theta} \end{aligned} \tag{3.2}$$

**Constitutive Equations**

$$\begin{bmatrix} \sigma_x \\ \sigma_\theta \\ \sigma_r \\ \gamma_{\theta r} \\ \gamma_{xr} \\ \gamma_{x\theta} \end{bmatrix} = \begin{bmatrix} \overline{C}_{11} & \overline{C}_{12} & \overline{C}_{13} & 0 & 0 & \overline{C}_{16} \\ \overline{C}_{12} & \overline{C}_{22} & \overline{C}_{23} & 0 & 0 & \overline{C}_{26} \\ \overline{C}_{13} & \overline{C}_{23} & \overline{C}_{33} & 0 & 0 & \overline{C}_{36} \\ 0 & 0 & 0 & \overline{C}_{44} & \overline{C}_{45} & 0 \\ 0 & 0 & 0 & \overline{C}_{45} & \overline{C}_{55} & 0 \\ \overline{C}_{16} & \overline{C}_{26} & \overline{C}_{36} & 0 & 0 & \overline{C}_{66} \end{bmatrix} \begin{bmatrix} \varepsilon_x \\ \varepsilon_\theta \\ \varepsilon_r \\ \gamma_{\theta r} \\ \gamma_{xr} \\ \gamma_{x\theta} \end{bmatrix} \tag{3.3}$$

At this point the expressions for stress, strain and displacement can be derived in terms of the transformed material stiffness matrix ($\overline{C}_{ij}$), $\varepsilon^0$, $\gamma^0$, $A_1$ and $A_2$. Since the elastic properties and geometric considerations are known for a given structure, the $\overline{C}_{ij}$ values can be calculated for each ply. The remaining unknown terms - $\varepsilon^0$, $\gamma^0$, $A_1$ and $A_2$ – need to be found using the boundary conditions. For a laminated structure composed of N layers, there will be 2N+2 unknowns – $\varepsilon^0$, $\gamma^0$, N $A_1$'s, and N $A_2$'s. The first boundary condition is a relation between the applied axial force and the axial stress. For a tube in axial tension, the applied axial force, $F_x$, must be equal to the sum of the integrals of the axial stress through the thickness. The same applies to a tube with an applied torque, $T_x$. The sum of the integrals of the shear stress must equal the applied torque. The expressions for these boundary conditions are:

$$\begin{aligned} F_x &= 2\pi \sum_{k=1}^{N} \int_{r_{k-1}}^{r_k} \sigma_x^{(k)}(r) r\, dr \\ T_x &= 2\pi \sum_{k=1}^{N} \int_{r_{k-1}}^{r_k} \tau_{x\theta}^{(k)}(r) r^2\, dr \end{aligned} \tag{3.4}$$

This gives two equations towards the 2N+2 unknowns. Two more come from the pressurized cylinder condition. The pressure at the inner and outer surfaces must be equal and opposite to the applied pressures. These can be equated as:

$$-p_i = \sigma_r^1(R_i)$$
$$-p_o = \sigma_r^N(R_o) \tag{3.5}$$

where $p_i$ and $p_o$ are in the applied internal and external pressures, $R_i$ and $R_o$ are the inner and outer radii, and the superscript on the stress expression is the layer of the material. The last two requirements for the tube are that of continuity of traction and displacements at ply interfaces, or:

$$w^{(k)}(r_k) = w^{(k+1)}(r_k)$$
$$\sigma_r^{(k)}(r_k) = \sigma_r^{(k+1)}(r_k) \tag{3.6}$$

This gives the last 2(N-1) equations needed to solve for the unknowns. Simultaneously solving the above equations will give the 2N+2 unknowns for the displacement, strain and stress equations.

### *3.2 Nonlinear Regression Analysis or "Inverse" Solution*

Now that an analytic expression exists, it is possible to develop a method using this model to back calculate the ply level properties. In a thesis by George, a nonlinear regression method was used to find the best ply level elastic properties to fit a set of experimental data[20]. Figure 3-1 illustrates the steps in the nonlinear regression analysis. In the first step, the sample geometry (number of plies, orientation, interfacial radii, etc...), guess values for the elastic properties ($E_1$, $E_2$, $E_3$, $G_{12}$, $\nu_{12}$, $\nu_{13}$, $\nu_{23}$, $\alpha_1$, $\alpha_2$ and $\alpha_3$), and the applied loads ($F_x$, $T_x$, $P_i$, $P_o$, and any combinations of each) are entered into the elasticity solution. The strain response ($\varepsilon_x$, $\varepsilon_\theta$ and $\gamma_{x\theta}$) for each load condition is calculated. At this point, there are two sets of strain values, the experimental data and those calculated from the guess values. The goal of the program is to minimize the error function, Y, which is defined as:

$$Y = \sum\sum\Phi^2 = \sum\sum(\varepsilon_m - \varepsilon_c)^2 \tag{3.7}$$

Where $\varepsilon_m$ and $\varepsilon_c$ are the measured and calculated strain values, and Y is the sum of square errors (SSE).

If the system of equations were linear, a minimum in the error function would be found in one step. Since this is not, a nonlinear regression technique must be used. The difference is that the nonlinear method is an iterative process, with each successive step decreasing the SSE. A solution is found by declaring convergence criteria, which can range from calculating if the variables are no longer changing, or defining a fixed number of iterations for the system. Usually, more than one of the criteria will be employed to reduce computation time and determine the conditions at convergence. Other criteria are chosen to stop the program if the system is not converging to a solution. This is dependent upon the quality of the data and guess values. If either is not sufficient, the system may not converge to a meaningful solution.

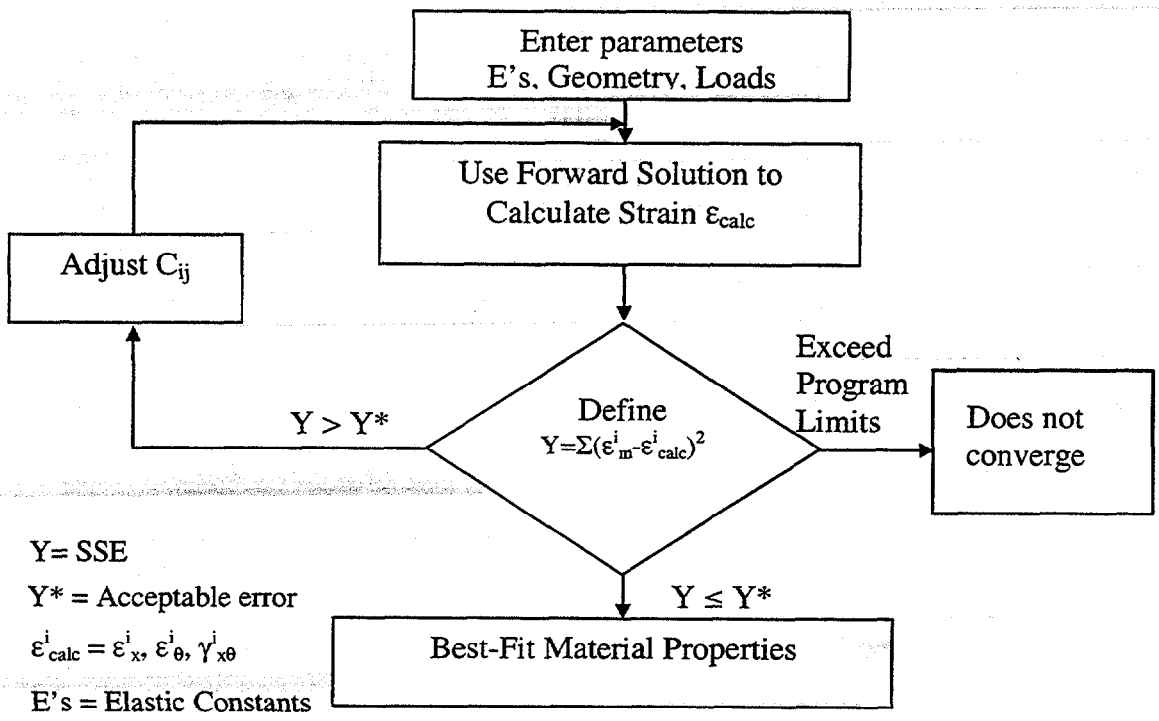


**Figure 3-1: Schematic of Inversion Program**

At this point, C++ codes have been written for the Forward and Inverse solutions. In order to test the method, a fictitious composite laminate data set was created, and the Forward solution was used to generate the strain response. The guess values were altered and input into the Inverse solution. Table VI contains the guess values, solution values and the correct values for the test run. The maximum number of iterations was set to 25, with no other criteria used, to obtain a plot of the variation in the SSE with each iteration, as seen in Figure 3-2. After each iteration, the values are improved and the sum of squared error decreases until the solution is found (the line plateaus). The different lines are for the number of significant digits included in the strain values used as the experimental data set. Truncating the strain values before they were input into the analysis controlled the number of significant digits, illustrating the effects of error on the input values. The effect is not significant for exact values (4 or more significant digits), but does introduce large errors in some of the values in the cases of 2 or 3 significant digits. This is not unexpected, linear and nonlinear regression are sensitive to error in the input values. This sensitivity is not desirable since the accuracy of experimental measurement cannot be expected to these levels.

**Table VI. Data set used in the Inversion Program (Input and Output are for 6 significant digits).**

| Value | Input Value | Output Value | Correct Value |
|---|---|---|---|
| $E_1$ | 10000 | 2.15E+07 | 2.15E+07 |
| $E_2$ | 1000 | 1.46E+06 | 1.46E+06 |
| $E_3$ | 1500 | 1.46E+06 | 1.46E+06 |
| $G_{12}$ | 5000 | 5.61E+06 | 5.61E+06 |
| $\nu_{12}$ | 0.1 | 0.3 | 0.3 |
| $\nu_{13}$ | 0.159 | 0.5896 | 0.59 |
| $\nu_{23}$ | 0.1 | 0.59 | 0.59 |

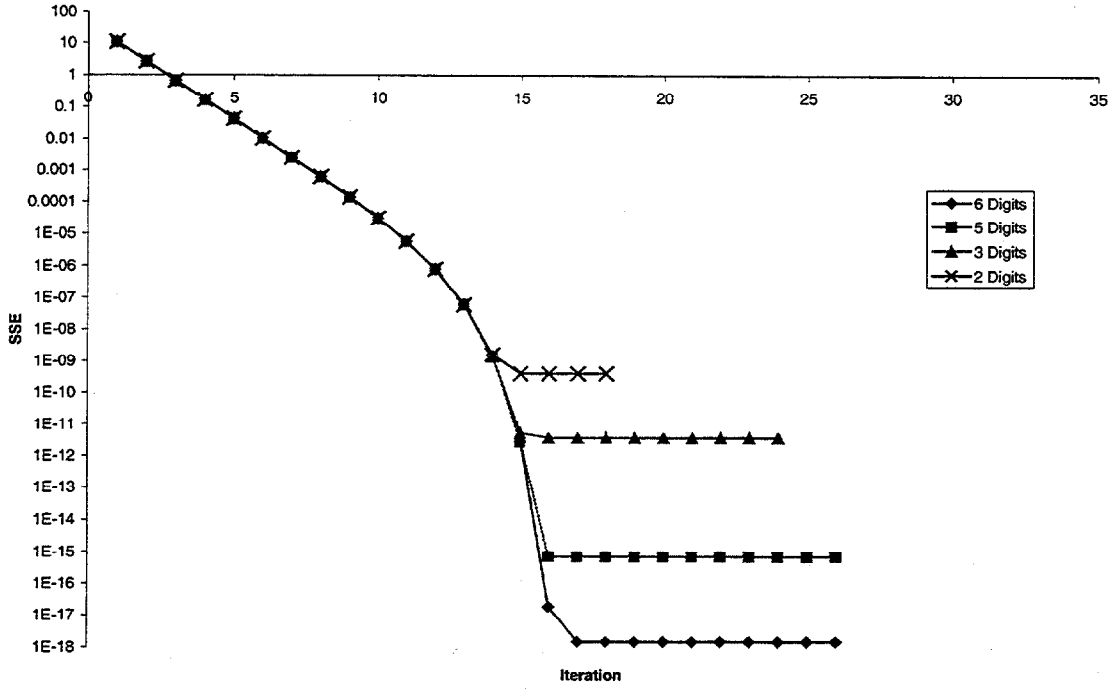


**Figure 3-2: Sum of Square Error values for each iteration**

The data described in Section 2 of this paper has been reduced for input into the analysis by fitting the linear elastic portions of the data with a best-fit line. The slopes of the data were used to calculate the strain response at the maximum and minimum load ranges for each of the tests (except for the internal pressure tests where one was taken at the maximum and second was taken at an intermediate pressure). The same number of

data points were included from each tests, so the results would not be biased towards one set of data.

There is a discrepancy between the model used and the experimental samples. The model was designed to describe the deformations in a laminated structure composed of orthotropic layers of various orientations. The experimental samples are a laminated structure with woven plies. To approximate the behavior of the woven plies, each layer is modeled as 2 cross ply layers. The resulting geometric structure inputs for CVI 1219 are in Table VII. The experimental inputs, loads and strains, are in Table VIII. The load conditions used for the analysis are external and internal pressure ($P_o$ and $P_i$), axial tension and compression, and axial torque. For each of the loading conditions, the observed strains are input as well.

**Table VII. Geometric inputs for CVI 1219**

| | |
|---|---|
| Inner radius- cm (in) | 2.5 (0.98) |
| Outer radius - cm (in) | 2.95 (1.16) |
| Number of Layers | 16 |
| Layer Thickness - cm (in) | 0.47 (0.187) |
| Orientation | ±45 |

**Table VIII. Experimental Applied Loads and Measured Strains**

| Loads | | | | Strain | | |
|---|---|---|---|---|---|---|
| $P_o$ (MPa) | $P_i$ (MPa) | Axial Load (kN) | Torque (N-m) | $\varepsilon_x$ | $\varepsilon_\theta$ | $\gamma_{x\theta}$ |
| 0 | 4.14 | 0 | 0 | -6.2E-05 | 0.000337 | 4.63E-05 |
| 0 | 6.21 | 0 | 0 | -9.4E-05 | 0.000506 | 6.94E-05 |
| 0 | 0 | -22.2 | 0 | -0.00018 | 9.51E-05 | -6.64E-07 |
| 0 | 0 | 22.2 | 0 | 1.84E-04 | -9.51E-05 | 6.64E-07 |
| 0 | 0 | 0 | -215 | -4.44E-06 | 3.99E-06 | -1.56E-04 |
| 0 | 0 | 0 | 215 | 4.44E-06 | -3.99E-06 | 1.56E-04 |

The results for different sets of start values are in Table IX. The values in Set 1 are rough estimates of the measured stiffness values listed in Table IV and Table V, while those in Set 2 are rough estimates calculated using micromechanics models for $E_1$ and $E_2$:

$$E_1 = V_f E_f + (1 - V_f) E_m \tag{3.8}$$

$$\frac{1}{E_2} = \frac{1-\sqrt{V_f}}{E_m} + \frac{\sqrt{V_f}}{E_f\sqrt{V_f} + \left(1-\sqrt{V_f}\right)E_m} \tag{3.9}$$

where $E_f$ and $E_m$ are the modulus of the fiber and the matrix and $V_f$ is the fiber volume fraction. The modulus values used for the SiC and the Nextel 610 fiber are 414 and 372 GPa*, respectively, and a fiber volume fraction of 0.32 was used. The input values used in Set 3 were solutions from another optimization technique using the values from Set 1 as start values.

**Table IX. Input and output values for CVI 1219**

| | Set 1 | | Set 2 | | Set 3 | |
|---|---|---|---|---|---|---|
| Properties GPa (Msi) | Input | Output | Input | Output | Input | Output |
| $E_1$ | *172 (25.0)* | 208 (30.1) | *414 (60.0)* | 175 (25.5) | *199 (28.8)* | 254 (36.9) |
| $E_2$ | *76 (11.0)* | 108 (15.7) | *276 (40.0)* | 141 (20.4) | *53 (7.67)* | 59 (8.59) |
| $E_3$ | *69 (10.0)* | 4964(720.0) | *276 (40.0)* | 1855 (269.0) | *77 (11.2)* | 155 (22.5) |
| $G_{12}$ | *62 (9.0)* | 65 (9.49) | *131 (19.0)* | 66 (9.55) | *33 (4.84)* | 62 (9.02) |
| $\nu_{12}$ | *0.15* | 0.27 | *0.1* | 0.21 | *-0.01* | 0.38 |
| $\nu_{13}$ | *0.15* | -0.13 | *0.15* | -0.07 | *0.23* | -0.67 |
| $\nu_{23}$ | *0.25* | 0.13 | *0.25* | 0.07 | *0.63* | 0.58 |
| Error (SSE) | | 7.66E-09 | | 7.59E-09 | | 8.27E-09 |

The output values are different for each set of starting values. The only value that is consistent is the shear modulus value. The other in-plane values (1-2 values) are calculated with a range of values that are acceptable, while the out-of-plane values are not. The through-thickness stiffness ($E_3$) ranges in value from 155 GPa to 4964 GPa (22.5 Msi to 720 Msi), while the two Poisson's ratios ($\nu_{13}$ and $\nu_{23}$) range from –0.67 to 0.58. These values are well outside the expected ranges for these values ($E_3 \approx E_2$ and $\nu_{12} \approx \nu_{13}$), and at this time no start values have been found that return all values in the expected ranges. This is not indicative that analysis has failed. Figure 3-3 through Figure 3-5 are the graphs of the experimental data plotted with the calculated results. In each graph, the experimental strain measurements are plotted as data points, while the model predictions are the lines. In all cases the model matches the data very closely, with the possible exception of the shear strain values in Figure 3-5.

At this point, the analysis is finding material properties that generate strain values that minimize the error between the measured and predicted values, but the properties are not all falling within accepted values. The largest single reason for this is the lack of data used in this method. As with linear regression work, nonlinear regression functions better with larger data sets. This current work is being performed on essentially 9 data points to optimize 7 variables. With the lack of data, error in the experimental values can cause large error in the optimized values, which is believed to be what has happened to the out-of-plain values.

The procedures are being adapted to increase the amount of new data by recording the surface strains on the inner surface of the sample as well as the outer. This will double the data recorded for the axial tests (both tension and torsion), and should allow for improved differentiation between the results as to which set better describes the

* Values taken from reports on the 3M website

data. Other possible problems are the difference in the structure (cross-ply layers approximating woven structures) from the model to the experimental samples and the existence of damage. Matrix cracking might cause the structure as a whole to deform in an inconsistent fashion to what would be predicted by all the elastic properties being within the acceptable ranges. These ideas are currently being researched in the hope of improving confidence in the solution values.

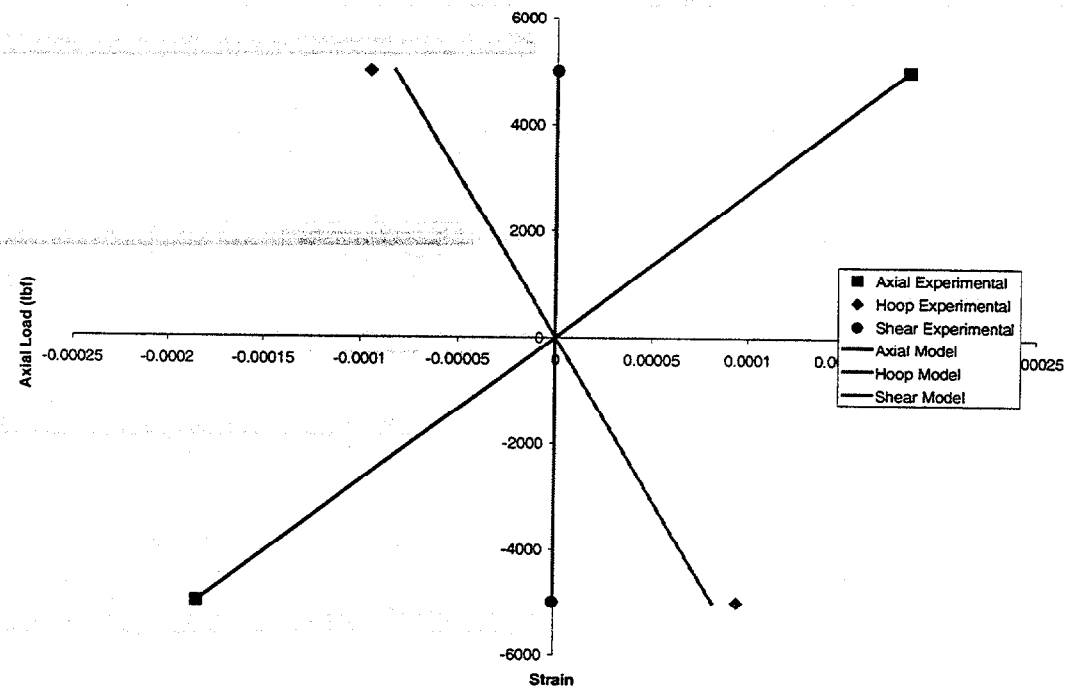


**Figure 3-3. Axial tension and compression results – the data points are the experimentally observed values and the lines are the model predictions**

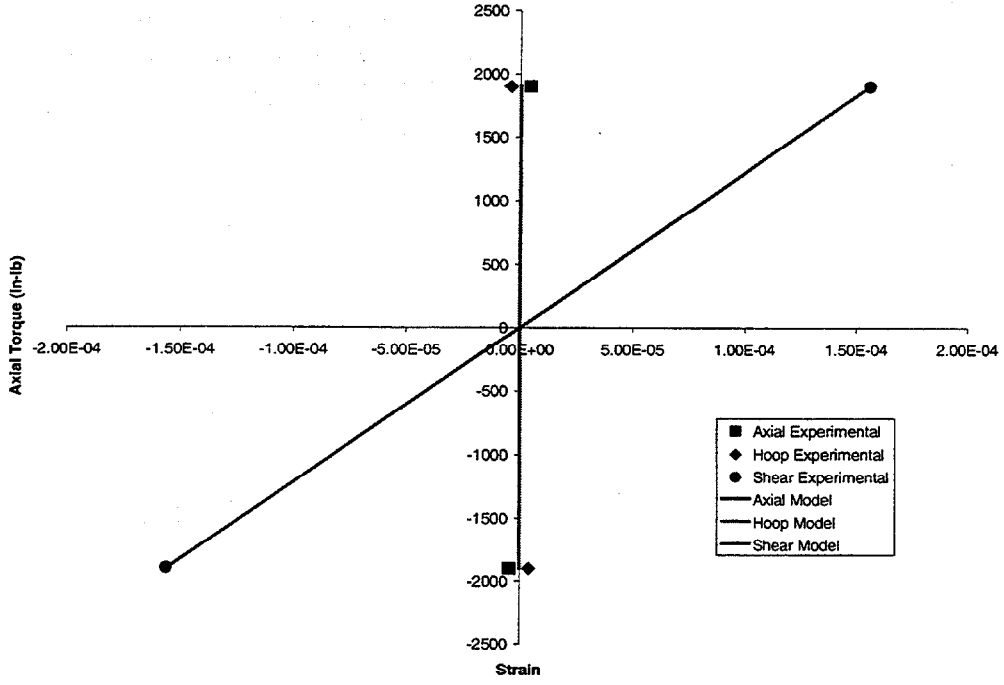


**Figure 3-4. Axial torsion results– the data points are the experimentally observed values and the lines are the model predictions**

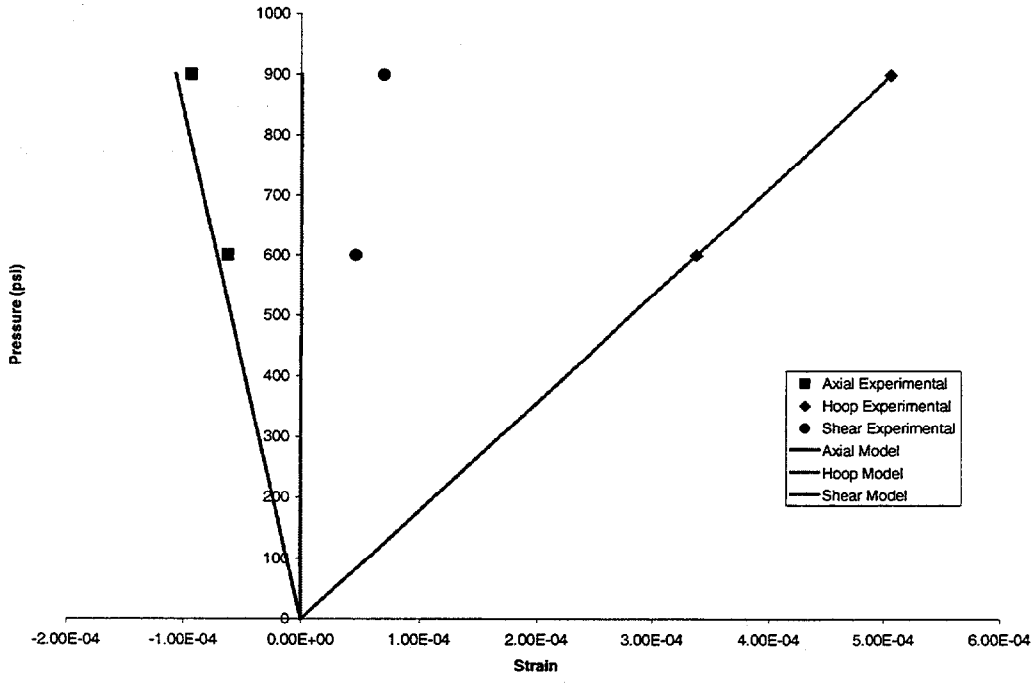


**Figure 3-5. Internal pressure results – the data points are the experimentally observed values and the lines are the model predictions**

# 4. Effect of Randomly Distributed Fibers on the Toughness of Fibril-Reinforced Composite Materials

## *4.1 Introduction*

Fossil environments will require materials that tolerate 1250 C and possibly higher temperatures. The mechanical properties of Nicalon and Nextel fibers deteriorate significantly at such temperatures. There has been a large effort to develop higher-temperature fibers. Unfortunately, these efforts have not been very successful. However, high-strength fibrils can be fabricated by the techniques such as the VLS techniques developed at Los Alamos National Laboratory[21]. The critical stress for extension of short (non-steady-state) matrix cracks bridged by continuous fibers parallel to the applied load and perpendicular to the crack has been thoroughly analyzed using fracture mechanics principles by Marshall et al.[22], McCartney[23], Majumdar et al.[24]. In their analysis, authors proceed by equating the effective stress intensity factor obtained for the matrix crack, i.e., the stress intensity factor obtained by superposing the contributions of the far field stress and of the crack bridging fiber tractions with an effective fracture toughness of composite. The computation involves three key steps:

1. Development of a relation between traction applied by the crack-bridging fibers and the crack-opening displacement;
2. Use the force displacement relation in an iterative numerical scheme to obtain a self-consistent crack opening profile and crack-bridging tractions at a given applied stress;
3. Use of the self-consistent fiber tractions to calculate the effective stress intensity factor and the critical stress based on an appropriate fracture criterion.

In this work, we extend the Marshall et al.[22] approach to the analysis of inclined and randomly distributed fibers within a composite specimen.

## *4.2 Crack Closure Pressure for an Inclined Fiber*

The mechanics of fiber pullout can be conveniently analyzed by applying tractions $T_m$ and $T_f$ equal and opposite to the stresses in the matrix and fibers along AA' at the end of the slipped region (as shown in Figure 4-1), and removing the section AA'CC'. If we neglect the effect of shear stresses above AA' (i.e., assume that it represents an isostrain plan) these tractions are related:

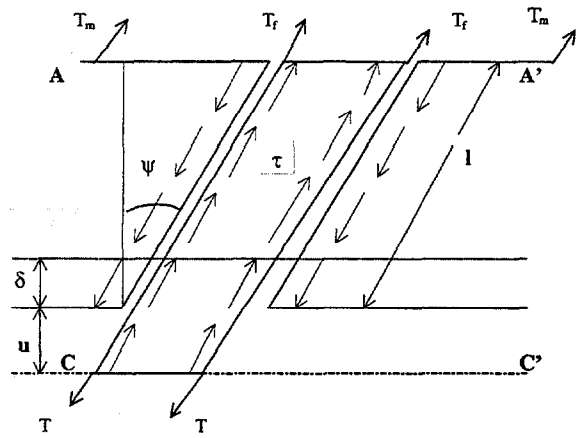


**Figure 4-1: Analysis of fiber pullout for an inclined fiber**

$$\frac{T_m}{E_m} = \frac{T_f}{E_f} \tag{4.1}$$

where,

$T_m$ and $T_f$ are the tractions within the matrix and the fiber respectively;
$E_m$ and $E_f$ are the modulus within the matrix and the fiber respectively.

Equations relating the stresses and displacements are obtained by considering the equilibrium of the matrix and fiber separately and also calculating the extensions δ and δ+u of the matrix and fiber Marshall et al.[22].

***Matrix equilibrium:***

$$T_m A_m \cos\psi = 2\pi R\tau \cos\psi \tag{4.2}$$

***Fiber equilibrium:***

$$T\, A_f \cos\psi = T_f\, A_f \cos\psi + 2\pi R\tau \cos\psi \tag{4.3}$$

***Matrix elongation:***

$$\frac{\delta}{l\,\cos\psi} = \frac{\pi R l \tau}{A_m E_m} \tag{4.4}$$

***Fiber elongation:***

$$\frac{\delta}{l\cos\psi} + \frac{u}{l\cos\psi} = \frac{T_f}{E_f} + \frac{\pi R l \tau}{A_m E_m} \tag{4.5}$$

where,

$\psi$ = *fiber angle*
$A_m$ = *area of matrix per fiber*
$A_f$ = *fiber cross-sectional area* $A_f = \pi R^2$

$R$ = *fiber radius*
$l$ = *sliding length*
$\tau$ = *shear stress*
$\delta$ = *elongation*
$u$ = *crack opening*

From Equations (4.1) and (4.2), we have

$$T_f = \frac{2\pi R l \tau}{A_m}\frac{E_f}{E_m} \tag{4.6}$$

From Equations (4.3) and (4.6), we have

$$T = \frac{2\ l\tau}{R}[1+\eta] \tag{4.7}$$

with

(4.8)

$$\eta = \frac{E_f\ A_f}{E_m\ A_m} = \frac{E_f\ V_f}{E_m\ V_m} \tag{4.9}$$

If we substitute Equations (4.4) and (4.6) into Equation (4.5) we find:

$$\frac{u}{l} = \frac{2\pi R l \tau\cos\psi}{A_m\ E_m} + \frac{\pi R l \tau\cos\psi}{A_f\ E_f} - \frac{\pi R l\tau\cos\psi}{A_m\ E_m} \tag{4.10}$$

After some simplification, we can find the sliding length l:

$$l^2 = \frac{u R E_f}{\tau(1+\eta)\cos\psi} \tag{4.11}$$

Finally, by combining Equations (4.7) and (4.11) we obtain the traction T:

$$T = \left[\frac{4\,u\,E_f\,\tau(1+\eta)}{R\cos\psi}\right]^{1/2} \tag{4.12}$$

## *4.3 Extension to Randomly Distributed Fibers*

### *4.3.1 No Possible Fiber Pull-Out*

We now seek to extend the solution for the closure traction to the analysis of cracks that are bridged by randomly oriented fibers. These fibers are assumed to be sufficiently long that pullout does not occur. For such a case, the probability density function describing the orientation of fibers in the matrix is defined as (with the normalization condition)

$$F(\psi) = \int_0^{\psi} f(\psi)\,d\psi$$
$$F\left(\frac{\pi}{2}\right) = 1 \tag{4.13}$$

If we consider $f(\psi)$ = constant (so that the distribution is completely random), we find that:

$$f(\psi) = \frac{2}{\pi} \tag{4.14}$$

Following Jain and Wetherhold[25], we introduce the auxiliary variable y′, which represents the signed distance from fibers' center of gravity to the crack plane. The required probability density is:

$$P[E_1 E_2] \tag{4.15}$$

where

$$E_1 = y' \in [y', y' + d\,y']$$
$$E_2 = \psi \in [\psi, \psi + d\,\psi]$$

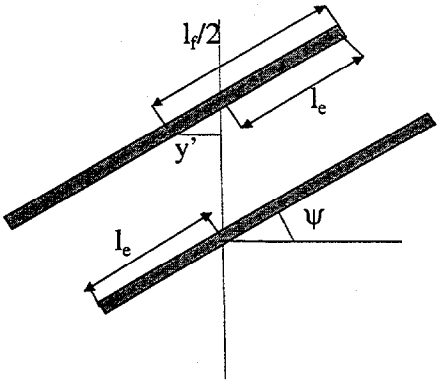


**Figure 4-2: Illustration of the definition of the auxiliary variable $y'$**

Using the Bayes' theorem for non-independent events $E_1$ and $E_2$ we can write:

$$P[E_1 E_2] = P\left[E_1 / E_2\right] P[E_2] \tag{4.16}$$

The second probability is well defined by Equation (4.14). For the events $E_1$ the only values of y′ of interest are those which intercept the crack, i.e. $y' \in \left[\frac{-l_f}{2}\cos\psi, \frac{l_f}{2}\cos\psi\right]$. Under the assumption that the fiber center of gravity is uniformly distributed in y direction $\left[f_y(y) = \frac{1}{h}, y \in [0, h]\right]$, we can say that y′ is also uniformly distributed $\left[f_{y'}(y) = \frac{1}{h}, y' \in [\Pi - h, \Pi]\right]$. We may study $y' \in \left[0, \frac{l_f}{2}\cos\psi\right]$ and multiply that probability by 2.

The probability density that a single fiber bridges an arbitrary crack plane $y' = \Pi$ with events $E_1$ and $E_2$ is thus:

$$dN_f = \begin{cases} \left(\frac{2}{\pi}\right)\left(\frac{2}{h}\right) d\psi dy' \\ 0 \ \ elsewhere \end{cases} \tag{4.17}$$

The number of fibers crossing the crack plane with events $E_1$ and $E_2$ is defined as:

$$N_{fc} = \left(\frac{2}{\pi}\right)\left(\frac{2}{h}\right) N_f \int_0^{\frac{\pi}{2}} \int_0^{\frac{l_f}{2}\cos\psi} d\psi dy' \tag{4.18}$$

where,

$h$ = *width of the composite plate*

$N_f$ = *total number of fiber in the sample.*

$$N_f = \frac{A_c h V_f}{A_f l_f} \tag{4.19}$$

The closure pressure is defined as:

$$P(y) = T(y) V_{fc} \cos^2 \psi \tag{4.20}$$

where,

$V_{fc} = \frac{A_f l_f}{A_c h} N_{fc}$ - Volume fraction of the fibers that bridge the crack plane $\Pi$ with events $E_1$ and $E_2$.

By taking into account Equation (4.18) and Equation (4.19) we can write:

$$V_{fc} = \left( \frac{2}{\pi} \frac{2}{h} \int_0^{\frac{\pi}{2}} \int_0^{\frac{l_f}{2}\cos\psi} d\psi dy' \right) V_f \tag{4.21}$$

Thus, if the crack is large enough that bridging fibers are randomly distributed, the approximate closure pressure as a function of position is given by

$$P(y) = A \int_0^{\frac{\pi}{2}} \int_0^{\frac{l_f}{2}\cos\psi} T(y) \cos^2 \psi dy' d\psi \tag{4.22}$$

where

$$A = \left(\frac{2}{\pi}\right)\left(\frac{2}{h}\right) V_f$$

$$T(y) = \left[ \frac{4u(y) E_f \tau (1+\eta)}{R \cos\psi} \right]^{1/2} \tag{4.23}$$

After integration we have

$$P(y) = BT'(y)\int_0^{\frac{\pi}{2}} \left(\sqrt{\cos\psi}\right)^5 d\psi \tag{4.24}$$

where

$$B = \left(\frac{2}{\pi}\right)\left(\frac{l_f}{h}\right)V_f$$
$$T'(y) = \left[\frac{4u(y)E_f\tau(1+\eta)}{R}\right]^{1/2} \tag{4.25}$$

If we evaluate the integrand numerically, we obtain the final result

$$P(y) \approx 0.457\left(\frac{l_f}{h}\right)\left[\frac{4u(y)E_f\tau(1+\eta)}{R}\right]V_f \tag{4.26}$$

So that for the case in which the length of the fibers is the same as the width of the composite, the average bridging stress is roughly half that which would be expected if the fibers were aligned with the loading direction.

### *4.3.2 Possible Fiber Pull-Out*

Using the geometric relationship shown in Figure 4-2, $y' = \left(\frac{l_f}{2} - l_e\right)\cos\psi$, where $l_e$ represents the embedded length. For the embedded length $l_e$ defined as:

$$l_e = \frac{l_f}{2} - \frac{y'}{\cos\psi} \tag{4.27}$$

We have the following conditions:

$$\begin{cases} if\ l_e \geq l\ \ p = p(y) \\ if\ l_e < l\ \ p = 0 \end{cases} \tag{4.28}$$

Taking into account these conditions in Equation (4.21), changing the inner boundary limit of integration to $\left(\frac{l_f}{2} - l\right)\cos\psi$ and integrating on $l$ rather than $y'$ the expression of the crack closure pressure with possible pullout is:

$$P(y) \approx 0.457\left(\frac{l_f}{h} - l\right)\left[\frac{4u(y)E_f\tau(1+\eta)}{R}\right]V_f \tag{4.29}$$

where $l$ is the sliding length defined by Equation (4.11).

Once the crack closure pressure is obtained, it is possible to determine the crack shape and the stress intensity factor at the crack tip as a function of the global applied load.

### *4.4 Crack Opening and Stress Intensity Factor*

The crack-opening displacement, u(Y), at any position is determined by the entire distribution of surface traction[26]:

$$u(Y) = C\int_Y^1 \frac{s}{\left(s^2 - Y^2\right)^{1/2}} \int_0^s \frac{\sigma_\infty - P(t)}{\left(s^2 - t^3\right)^{1/2}} dtds \tag{4.30}$$

where

$$C = \frac{4\left(1-\nu^2\right)c}{\pi E_c} \tag{4.31}$$

$\nu$ = *Poisson's ratio*
$c$ = *half crack length*
$E_c$ = *composite module*
$Y$ = *normalized position coordinate, y/c*
$\sigma_\infty$ = *far field stress*
$P$ = *crack closure pressure*

By superposing the contribution of the far field and the crack closure pressure, we obtain the expression of the stress intensity factor as follows [26]:

$$K = 2\left(\frac{c}{\pi}\right)^{1/2} \int_0^1 \frac{\sigma_\infty - P(Y)}{\left(1-Y^2\right)^{1/2}} dY \tag{4.32}$$

It is essential to ensure that the crack-opening displacement and the crack closure pressure are self-consistent with each other before any computation of the stress intensity factor. This can be achieved using numerical techniques. In this paper we used the same numerical procedure as Marshall et al.[22].

### *4.5 Numerical Procedure*

Equation (4.30) is solved numerically using an iterative procedure. The value of the crack opening is used to compute the corresponding crack closure pressure, which will give the value of the crack opening for the next iteration. The value of u(Y) was computing at $Y = \sin\left(\frac{i*\pi}{2*n}\right)$, where $i$ varies from 1 to n and n is the number of interval in y. We consider that the convergence to self-consistency achieved as follows:

> *If the value of the crack opening, $u_n$, used at iteration n to compute led to the value, $u'_n$, then the value to be tried at the iteration (n+1) was $\alpha u_n + (1-\alpha)u'_n$ where the damping coefficient $\alpha$ is set to 0.5 for short cracks and higher for larger cracks. This process was continued till the difference between the values of two successive iterations is less than a tolerance fixed by the user.*

Figure 4-3 and 4 show examples where the crack opening u and the crack closure pressure $P$ are compared with those when the fibers are straight.

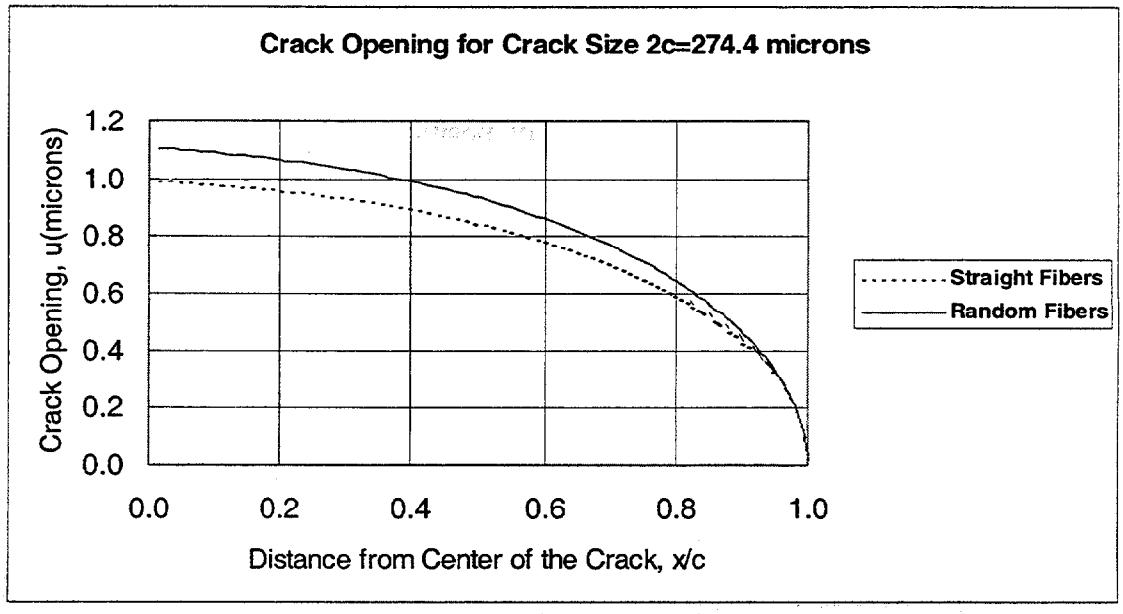


**Figure 4-3. Crack opening displacement for composites reinforced with aligned fibers and randomly oriented fibers.**

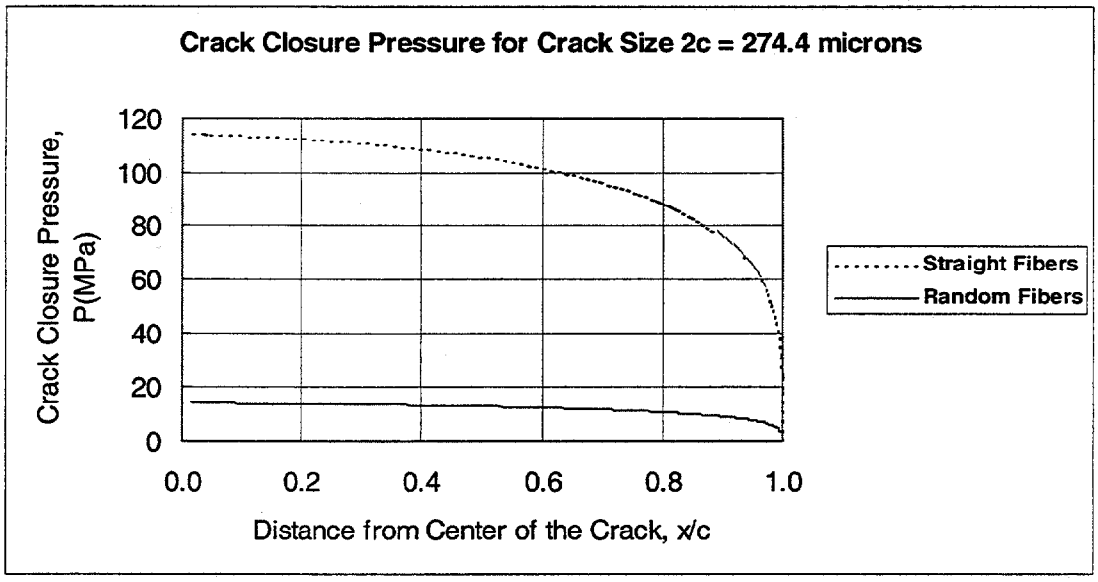


**Figure 4-4. Crack closure pressure for composites reinforced with aligned fibers and randomly oriented fibers.**

The sample dimension and the matrix and fiber properties used in the analysis are summarized in Table 10 and Table 11. In Figure 4-4, we see the strong influence of the fiber orientation on the crack closure pressure—a direct measure of the effectiveness of the fiber reinforcement.

**Table 10: Dimensions Used in Analysis**

| Length (cm) | Width (cm) | Thickness (cm) |
|---|---|---|
| 15 | 2.5 | 0.25 |

**Table 11: Summary of Fiber and Composite Properties**

| Property | Fiber | Matrix |
|---|---|---|
| $E(MPa)$ | 428 | 222 |
| $\nu$ | 0.2 | 0.24 |
| $R(\mu m)$ | 72 | |
| Volume Fraction | 0.21 | 0.79 |
| $K_c\left(MPa*\sqrt{m}\right)$ | N/A | 2.7 |

Finally, we examined the effect of fiber length in the case of possible fiber pullout. As we expected the longer the fiber is the bigger the closure pressure is. These results are represented in Figure 4-5 for three different lengths.

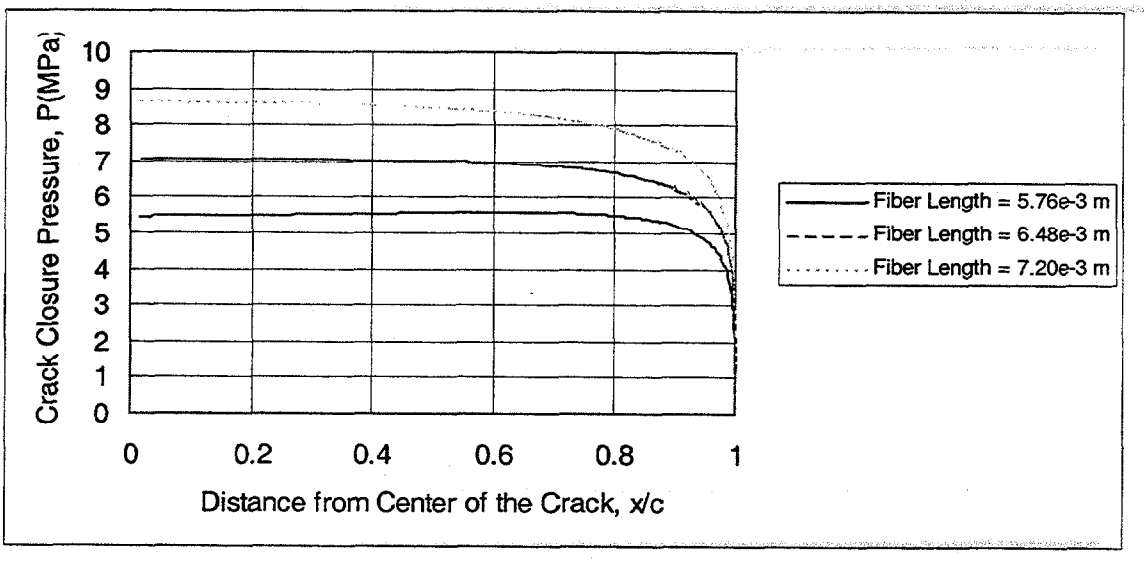


**Figure 4-5. Crack closure pressure for composites containing randomly oriented short fibers as a function of fiber length.**

The results of the analysis can also be used to determine the apparent toughness of the composite as a function of crack size. Such a result is shown in Figure 4-6.

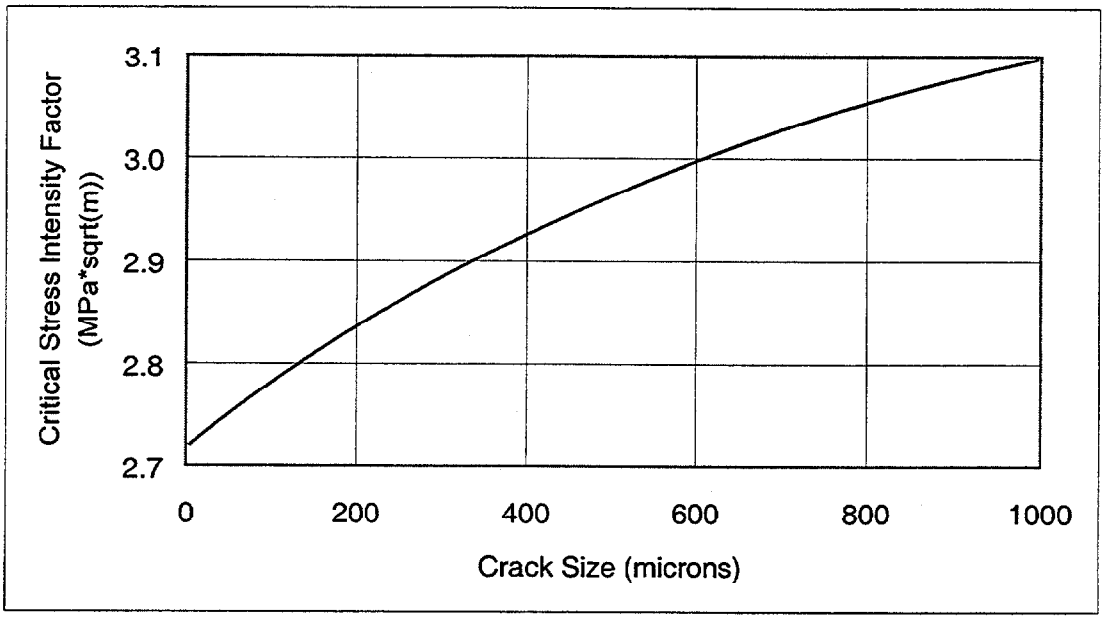


**Figure 4-6. Critical stress intensity factor as a function of crack size.**

## 5. Summary

In this report, we have provided mechanical assessment of structural tube components fabricated using the FCVI process. Failed specimens exhibited fiber pullout. Those failed samples that did not fail in the grips also exhibited non-linear stress-strain behaviors. Strengths exhibited by these tubes were superior to those measured previously for Nicalon/SiC and alumina/alumina ceramic composites of various designs and lay-ups. In addition, we have developed a modeling approach for extracting ply-level properties from the tests conducted on tubular materials. These properties may then be related to local details (such a porosity) to gain a greater understanding of the factors affecting the tubular performance.

Our analysis of the composites reinforced by fibrils shows that the fibrils can be effective in increasing the toughness of the composites through crack bridging and eventual pullout. We find that the fibrils (as expected) are most effective when aligned with the direction of loading, but that then can still provide an increase in apparent critical stress intensity factor when randomly oriented.

The above accomplishments provide the Fossil Energy program, and other industrial developers of CMC's with (i) a solid base of knowledge of the mechanical properties of composite tubes fabricated using the FCVI technique, (ii) an analysis for developing the ply-level properties of such tubular composites based upon the global performance, and (iii) a model for assessing the efficacy of randomly oriented fibrils for improving the toughness of CMC's. Each of these advances are important steps in the path from successful material processing to component design and component performance that are required for the ultimate development of operating ceramic components in fossil energy applications.

## 6. References


1. T. Besmann, B. W. Sheldon, R. A Lowden, and D. P. Stinton, "Vapor-Phase Fabrication and Properties of Continous-Filament Ceramic Composites," *Science*, 253, pp 1104-1109, 1991.

2. K. J. Probst, T. M. Besmann, D. P. Stinton, T. J. Anderson, and T. L. Starr, "Recent Advances in Forced-Flow, Thermal Gradient CVI for Refractory Composites," *Surface Coatings and Technology*, 120-121, pp. 250-258, 1999.

3. K. J. Probst, T. M. Besmann, J. C. McLaughlin, T. J. Anderson, and T. L. Starr, "Development of a Scaled-Up Chemical Vapor Infiltration System for Tubular Geometries," *Materials at High Temperatures*, 16[4], pp. 201-205, 1999.

4. B. L. Weaver, R. A. Lowden, J. C. Laughlin, D. P. Stinton, T. M. Besmann and O. J. Schwarz, "Nextel/SiC Composites Fabricated Using Forced Chemical Vapor Infiltration," *Ceramic Engineering and Science Proceedings*, 14[9-10], pp. 1008-1015, 1993.

5. K. R. Vaidyanathan, J. Sankar, A. D. Kelkar and B. Weaver," Mechanical Properties of Nextel 312 Fiber-Reinforced SiC Matrix Composites in Tension," *Ceramic Engineering and Science Proceedings*, 15[4], pp. 251-261, 1994.

6. K. R. Vaidyanathan, J. Sankar, A. D. Kelkar and J. Narayan, "Investigation of Mechanical Properties of Chemically Vapor Infiltrated (CVI) Ceramic Matrix Composites," *Ceramic Engineering and Science Proceedings*, 15[4], pp. 281-291, 1994.

7. K. R. Vaidyanathan, J. Sankar, A. D. Kelkar, D. P. Stinton and M. H. Headinger, "Investigation of Mechanical Properties of Chemically Vapor Infiltrated Ceramic Matrix Composites Under Pure Tension, " *Ceramic Engineering and Science Proceedings*, 14[9-10], pp. 1016-1027, 1993.

8. K. Liao, E. George, and K. L. Reifsnider, "Characterization of Ceramic Matrix Composite Tubes Under Uniaxial/Biaxial Monotonic and Cyclic Loading," *Proceedings of the 1995 Symposium on Multiaxial Fatigue and Deformation Testing Techniques, ASM STP 1280*, pp. 224-240, 1997.

9. K. Liao, M. Elahi, and K. L. Reifsnider, "Uniaxial and Multiaxial Fatigue of Ceramic Composite Tubes," *Ceramic Engineering and Science Proceedings*, 16[4], pp. 559-569, 1995.

10. K. L. Reifsnider, W. W. Stinchcomb, L. Olesksuk, and S. S. Lee, "Investigation of Properties and Performance of Ceramic Composite Components," *Proceedings of the Eigth Annual Conference on Fossil Energy Materials*, May 10-12, 1994, Oak Ridge, TN, pp. 19-28, 1994.

11. X. Huang, R. H. Carter, and K. L. Reifsnider, "Experimental Study and Modeling of a Novel Ceramic Composite Hot Gas Candle Filter Material," *Ceramic Engineering and Science Proceedings*, **19** [3], (1998).

12. R. H. Carter, X. Huang, and K. L. Reifsnider, "Experimental Study of a Ceramic Hot Gas Candle Filter,"*Ceramic Engineering and Science Proceedings*, **20** [3], pp. 153-160, 1999.

13. J. P. Singh, M. Sutaria, and W. Bielke, "Thermal Shock Behavior of Advanced Ceramic/Composite Hot-Gas Filters" *Ceramic Engineering and Science Proceedings*, **18**[3], pp.719-727, 1997.

14. L. Chuck and G. Graves, "Hoop Tensile Strength and Fracture Behavior of Continuous Fiber Ceramic Composite (CFCC) Tubes from Ambient to Elevated Temperatures," *Journal of Composites Technology & Research*, Vol. 19, No. 3, pp. 184-190, 1997.

15. Personal Communications with E. Lara-Curzio, Oak Ridge National Laboratory, January, 2001.

16. S. P. Timoshenko and J. N. Goodier, *Theory of Elasticity*, McGraw-Hill, Inc., New York, NY, pp. 68-69, 1970.

17. N. E. Dowling, *Mechanical Behavior of Materials*, Prentice-Hall, Inc., Englewood Cliffs, NJ, pp. 162-164, 1993.

18. I. M. Ward and D. W. Hadley, *An Introduction to the Mechanical Properties of Solid Polymers*, John Wiley and Sons, New York, 1993.

19. C. Rousseau, M. Hyer, and S. Tompkins, *Stresses and Deformations in Angle-Ply Composite Tubes*, Center for Composite Materials and Structures report #CCMS-87-04, Virginia Tech, Blacksburg, VA, 1987.

20. E. George, E. A *Method for the Ply-Level elastic Characterization of Composite Materials Using Thick Tubular Angle-Ply Specimens*, M.S. Thesis, Virginia Tech, Blacksburg, VA, 1993.

21. W. E. Hollar, G. P. DeMunda, J. J. Kim, and W. H. Mills, "Engineering Scale Development of the Vapor-Liquid Solid (VLS) Process for the Production of Silicon Carbide Fibrils," *Ceramic Engineering and Science Proceedings*, **14** [7-8], pp. 512-520, 1993.

22. D. B. Marshall, B. N. Cox, A. G. Evans, "The Mechanics of Matrix Cracking in Brittle-Matrix Fiber Composites," *Acta Metall.*, 33[11], pp. 2013-2021, 1985.

23. L. N. McCartney, "Mechanics of Matrix Cracking in Brittle- Matrix Fiber Reinforced Composites," *Proc. R. Soc. London*, A. 409, pp. 329-350, 1987.

24. B. S. Mujumdar, G. M. Newaz, and M. D. Thouless, "Yielding Behavior of Ceramic Matrix Composites," *Advances in Fracture Research, Proceedings of 7th International Conference on Fracture (ICF7)*, Edited by K. Salama, K. Ravi Chandar, D. M. R. Taplin, and P. Rama Rao, Pergamon Press, Oxford, UK, pp. 2805-2814, 1989.

25. L.K. Jain, R.C. Wetherhold, "The Effect of Fiber Orientation on the Fracture Toughness of Brittle Matrix Composites", *Acta. Metall. Mater*, 40 [6], pp. 1135-1143, 1992.

26. I. N. Sneddon and M. Lowengrub, *Crack Problems in the Classical Theory of Elasticity*, pp. 25-28, Wiley, New York, 1969.

**DISTRIBUTION**

3M COMPANY
Ceramic Materials Department
201-4N-01 3M Center,
St. Paul, MN 55144
M. A. Leitheiser

ALBANY RESEARCH CENTER
1450 Queen Avenue, SW
Albany, OR 97321
R. P. Walters

ARGONNE NATIONAL LABORATORY
9700 S. Cass Avenue
Argonne, IL 60439
W. A. Ellingson

BOSTON UNIVERSITY
Manufacturing Engineering
44 Cummington Street
Boston, MA 02215
V. Sarin

DOE
NATIONAL ENERGY TECHNOLOGY LABORATORY
3610 Collins Ferry Road
P.O. Box 880
Morgantown, WV 26507-0880
R. C. Bedick
D. C. Cicero
R. A. Dennis
N. T. Holcombe
W. J. Huber
T. J. McMahon
J. E. Notestein

DOE
NATIONAL ENERGY TECHNOLOGY LABORATORY
626 Cochrans Mill Road
P.O. Box 10940
Pittsburgh, PA 15236-0940
A. L. Baldwin
G. V. McGurl
U. Rao
R. B. Read
L. A. Ruth
T. M. Torkos

DOE
DOE OAK RIDGE OPERATIONS
P. O. Box 2008
Building 4500N, MS 6269
Oak Ridge, TN 37831
M. H. Rawlins

DOE
OFFICE OF FOSSIL ENERGY
FE-72
19901 Germantown Road
Germantown, MD 20874-1290
F. M. Glaser

LAWRENCE LIVERMORE NATIONAL LABORATORY
P.O. Box 808, L-325
Livermore, CA 94550
W. A. Steele

NATIONAL MATERIALS ADVISORY BOARD
National Research Council
2101 Constitution Avenue
Washington, DC 20418
K. M. Zwilsky

OAK RIDGE NATIONAL LABORATORY
P.O. Box 2008
Oak Ridge, TN 37831
B. Armstrong
T. M. Besmann
P. T. Carlson
J. M. Crigger **(2 copies)**
R. R. Judkins
D. P. Stinton

REMAXCO TECHNOLOGIES, INC.
1010 Commerce Park Drive
Suite I
Oak Ridge, TN 37830
R. D. Nixdorf

SHELL DEVELOPMENT COMPANY
WTC R-1371
P.O. Box 1380
Houston, TX 77251-1380
W. C. Fort

THE NORTON COMPANY
High Performance Ceramics Division
Goddard Road
Northborough, MA 01532-1545
N. Corbin

UNIVERSITY OF LOUISVILLE
Dept of Chemical Engineering
Speed Scientific School
Louisville, KY 40292
T. L. Starr

UNIVERSITY OF NORTH DAKOTA
Energy and Environmental Research Center
15 North 23rd Street
Grand Forks. ND 56202
J. P. Hurley

VIRGINIA POLYTECHNIC INSTITUTE & STATE UNIVERSITY
Department of Materials Engineering
Blackburg, VA 24601
K. L. Reifsnider

WESTINGHOUSE ELECTRIC CORPORATION
Research and Development Center
1310 Beulah Road
Pittsburgh, PA 15235-5098
S. C. Singhal